

Review Article

Open Access



Laser-induced direct graphene patterning: from formation mechanism to flexible applications

Haiyang Yu^{1,2}, Mengxin Gai^{1,2}, Lei Liu^{1,2}, Furong Chen^{1,2}, Jing Bian^{1,2,3,*}, Yongan Huang^{1,2,*}

¹State Key Laboratory of Digital Manufacturing Equipment and Technology, Huazhong University of Science and Technology, Wuhan 430074, Hubei, China.

²Flexible Electronics Research Center, Huazhong University of Science and Technology, Wuhan 430074, Hubei, China.

³College of Electronic and Optical Engineering & College of Flexible Electronics (Future Technology), Nanjing University of Posts and Telecommunications, Nanjing 210023, Jiangsu, China.

***Correspondence to:** Prof./Dr. YongAn Huang, State Key Laboratory of Digital Manufacturing Equipment and Technology, Huazhong University of Science and Technology, No. 1037 Luoyu Street, Hongshan District, Wuhan 430074, Hubei, China. E-mail: yahuang@hust.edu.cn; Dr. Jing Bian, College of Electronic and Optical Engineering & College of Flexible Electronics (Future Technology), Nanjing University of Posts and Telecommunications, No. 9 Wenyuan Road, Xianlin University Town, Nanjing 210023, Jiangsu, China. E-mail: jsbianjing@njupt.edu.cn

How to cite this article: Yu H, Gai M, Liu L, Chen F, Bian J, Huang Y. Laser-induced direct graphene patterning: from formation mechanism to flexible applications. *Soft Sci* 2023;3:4. <https://dx.doi.org/10.20517/ss.2022.26>

Received: 31 Oct 2022 **First Decision:** 16 Nov 2022 **Revised:** 6 Dec 2022 **Accepted:** 16 Dec 2022 **Published:** 19 Jan 2023

Academic Editor: Cunjiang Yu **Copy Editor:** Fangling Lan **Production Editor:** Fangling Lan

Abstract

Laser-induced graphene (LIG), which is directly fabricated by laser carbonization of polymers, has gained much attention in recent years since its first discovery in 2014. Specifically, featuring native porosity, good mechanical properties, and excellent electrical/electrochemical properties, it is considered a promising material for flexible electronic devices. Meantime, LIG can be processed in the atmosphere within a few seconds, thereby significantly reducing the fabrication cost of graphene. Facilitated by these features, this methodology has received great development with worldwide efforts in the following years, including the formation mechanism of LIG, the diversity of laser sources (from infrared laser to ultraviolet laser), the diversity of carbon sources (thermoset polymers, thermoplastic polymers, and natural polymers), and property modulation of LIG (porosity, electrical property, hydrophilic/hydrophobic property, electrochemical property), along with the broad applications of LIG in various flexible electronic devices. Here, the recent advances in the mechanism studies and preparation methods of LIG are comprehensively summarized. The various technologies for the modification of LIG are reviewed. A thorough overview of typical LIG-based flexible electronic devices is presented. Finally, the current challenges and future directions are discussed.



© The Author(s) 2023. **Open Access** This article is licensed under a Creative Commons Attribution 4.0 International License (<https://creativecommons.org/licenses/by/4.0/>), which permits unrestricted use, sharing, adaptation, distribution and reproduction in any medium or format, for any purpose, even commercially, as long as you give appropriate credit to the original author(s) and the source, provide a link to the Creative Commons license, and indicate if changes were made.



Keywords: Laser-induced graphene, flexible electronics, laser carbonization, flexible sensor

INTRODUCTION

Graphene, which is composed of hexagonal carbon atoms, has attracted much attention for its outstanding mechanical, optoelectronic, and electromagnetic properties^[1-4]. As a diverse material, graphene is a promising material for flexible electronics because it can be prepared on arbitrary flexible substrates without relying on complicated silicon-based semiconductor technology^[5-7]. The earliest graphene was prepared via the method of mechanical exfoliation^[8-11], and the graphene obtained by this method is inefficient and poorly controllable^[12]. With the rapid advancement in fabrication methods, graphene can be prepared by various technologies, such as chemical vapor deposition^[13-16], epitaxial growth^[17-20], and modification of graphene oxide^[21-23]. Although some methods (e.g., chemical vapor deposition and epitaxial growth) can prepare graphene with high quality, the high temperature and complicated patterning process severely limit their applications in flexible electronic devices^[24]. In most cases, modification of graphene oxide is considered a promising method for the preparation of flexible electronics because it can be produced on a large scale by solution processing methods^[25-27]. However, the environmental pollution caused by the massive use of chemical reagents in the fabrication of precursors limits its further application on electronic devices^[28].

Recently, a novel method of laser-induced carbonization has emerged to directly fabricate laser-induced graphene (LIG) on various flexible substrates with high precision (linewidth of 10 μm), high efficiency (preparation time of several seconds), and no chemical pollution (no chemical agents)^[29-31]. The resultant LIG shows native porosity, excellent thermal stability ($> 900\text{ }^\circ\text{C}$), high electrical conductivity (5-25 S/cm), and adjustable properties^[29]. Compared to traditional methods, this new method can be performed in the atmosphere, and the patterned graphene can be easily accomplished with computer programming techniques, thus greatly simplifying the preparation procedures and reducing costs^[32-34]. The initial laser source is a carbon dioxide laser with a wavelength of 10.6 μm ^[29,35], whose far-infrared property results in the deep ablation thickness of polymer and wide linewidth of LIG^[36-39]. To fabricate the thinner flexible electronics with smaller linewidth, selecting a laser with shorter wavelengths (e.g., 355 nm^[40,41]) and controlling process parameters are two common methods, which enable the fabrication of the visually invisible LIG with a linewidth of 10 μm ^[42]. Besides, any desired LIG pattern can be directly fabricated on various flexible substrates, including polyimide^[43,44], polyethylene terephthalate^[45], PDMS^[46-48], and flexible cellulose paper^[49-51]. In particular, the properties of LIG, including hole size, hydrophilic/hydrophobic, and square resistance, have been proven to be adjustable^[52,53]. These features promote the broad applications of this processing method in the fabrication of LIG-based flexible electronics^[54].

Although several excellent reviews have been published, the detailed formation mechanism of LIG under various laser sources and process parameters has rarely been summarized. Meanwhile, the property modulation and its applications in flexible electronic devices have also not been comprehensively reviewed. In this review, we mainly focus on the recent advances in the formation mechanism of LIG, property modulation methods, and their applications in flexible electronic devices [Figure 1]. Much attention has been first devoted to the formation mechanism of LIG under various photothermal or photochemical effects. On this basis, the diversity of laser and carbon sources and various methods of property modulation are reviewed, which helps researchers to select appropriate lasers, carbon sources, and processing schemes. The simple processing procedures and tunable properties of LIG have greatly facilitated the application of LIG-based flexible electronics, including actuators (e.g., photothermal actuators, and electrothermal actuators), sensors (e.g., strain sensors, gas sensors, and pressure sensors), electromagnetic devices (e.g.,

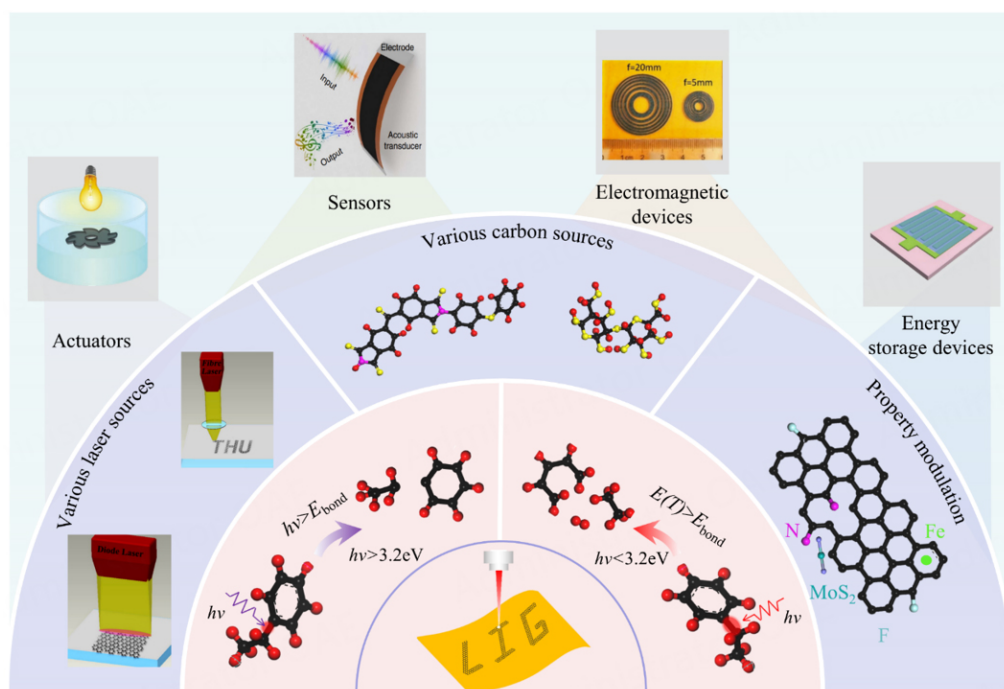


Figure 1. Recent advances in laser-induced graphene and its application for flexible electronic devices. Various laser sources^[34]. Copyright 2014, Elsevier. LIG-based flexible electronic devices consist of actuators [e.g., photothermal actuators^[100] (Copyright 2017, WILEY-VCH Verlag GmbH & Co. KGaA, Weinheim.)], sensors [e.g., acoustic sensors^[145] (Copyright 2017, The Author(s), published by Nature.)], electro magnetic devices [e.g., terahertz imaging devices^[80] (Copyright 2020, Optical Society of America)], and energy storage devices [e.g., supercapacitor^[168] (Copyright 2019, WILEY-VCH Verlag GmbH & Co. KGaA, Weinheim)].

radiofrequency antenna devices, electromagnetic shielding devices, wave modulators, and terahertz imaging devices), and energy storage devices (e.g., nanogenerators, supercapacitors, and batteries). Finally, the current challenges of LIG and future development directions are discussed.

FORMATION MECHANISM OF LIG

Photothermal and photochemical effects

When a laser is irradiated on the surface of the polymer, the polymer will absorb the laser energy to decompose at the irradiated position. Previous threshold studies have demonstrated that photon energies greater than 3.2 eV (wavelength less than 390 nm) can directly break the chemical bond of the polymer^[55]. Hence, according to the mechanism of laser-polymer interaction, it can be classified into two types: (1) photothermal-dominated polymer pyrolysis; and (2) combined photothermal and photochemical polymer pyrolysis.

For lasers with wavelengths larger than 390 nm, numerous experimental results demonstrate polymer pyrolysis is mainly based on the photothermal effect^[56-58]. During the photothermal process, the photon energy is less than the chemical bonds of the polymer, such as C-O, C-N, and C=O^[59], but the absorbed photons cause faster atomic vibration to heat up the local area [Figure 2A]^[60]. This heating effect leads to the breaking of chemical bonds when the absorbed energy exceeds the bond energy. To accurately illustrate this process, a theoretical photothermal model was established as $d = k \times e^{-E/RT}$ ^[61], where the ablation rate d is mainly determined by a combination of the Arrhenius index factor k , activation energy E , gas constant R , and the average temperature of the laser-radiated region. The first three parameters are constants for a given material. The last parameter is affected by multiple factors, including laser power, scanning speed,

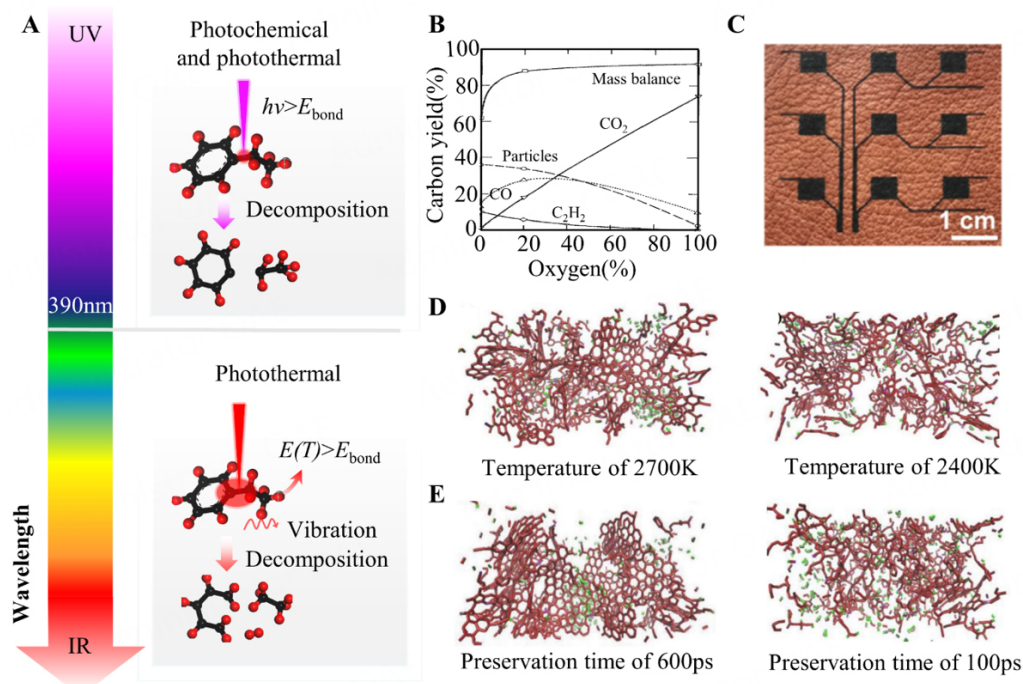


Figure 2. Mechanism of the formation of LIG. (A) Schematic diagram of the preparation of LIG at different wavelengths. (B) Variation of carbon yield with oxygen^[74]. Copyright 1989, published by AIP Publishing. (C) Photograph of carbonized sensor array^[82]. Copyright 2020, WILEY-VCH Verlag GmbH & Co. KGaA, Weinheim. (D) Distributions of carbon atoms at 2700 K and 2400 K. (E) Distributions of carbon atoms at preservation times of 600 ps and 100 ps. Reproduced with permission^[83]. Copyright 2019, WILEY-VCH Verlag GmbH & Co. KGaA, Weinheim.

absorbance, and sample structure. Generally, with the increase in laser power or the decrease in scanning speed, the average temperature of the laser-radiated region increases^[62,63]. The well-matched manner (high absorbance for the laser) of the polymer and the laser can effectively improve the utilization of the laser, allowing the required temperature of LIG at low power density^[64]. Besides, sample structures (surface ablation and interface ablation) also have a significant effect on the average temperature of the laser-radiated region^[65]. Compared to surface ablation, interface ablation shows a highly concentrated temperature distribution due to the heat conduction of the top substrate.

As for the laser with photon energies greater than 3.2 eV, polymer pyrolysis is generally considered to be a coupling of photothermal and photochemical effects [Figure 2A]^[66]. Unlike the local heating of the photothermal effect, the photochemical effect can directly break some chemical bonds with bond energy less than photon energy^[67,68]. Polymer carbonization occurs when the absorbed photon concentration exceeds the threshold photon concentration, which is a constant for a given material. At low laser fluence ($< 1 \text{ J/cm}^2$), the ablation rates predicted by the pure photochemical effect are in good agreement with the experimental data^[69]. With the increase of laser fluence, the discrepancy between theory and experiment is more pronounced due to the non-negligible temperature rise effect caused by molecular energy levels and radiation-free leap processes for the short wavelength lasers ($< 390 \text{ nm}$)^[70,71]. Therefore, a combined photothermal-photochemical effect is proposed by Babu *et al.*, which is in good agreement with experimental data over a wide range (e.g., 0 to 100 J/cm^2 for a 248 nm KrF laser)^[66].

Carbonization mechanisms of polymers

At the irradiated zone, high-temperature (> 2700 K) and high-pressure (~ 3 GPa) environments are formed on the surface of the polymer, which results in the breakage and reuniting of polymer molecules^[72,73]. In this process, the residual solid product is generated with some gases (e.g., CO, CO₂, and C₂H₂ in [Figure 2B](#))^[74-76]. The release of gas leads to the formation of the porous feature of the residual solid product^[77,78].

There is a threshold power density for the formation of LIG with a D peak (defect peak), a G peak (vibration of sp² carbon atoms), and a 2D peak (vibration between layers) of the Raman spectrum. Due to different mechanisms of laser-polymer interaction, this threshold is different for various laser sources, such as 5.5 J/cm² for 10.6 μm laser^[79] and 8.75 J/cm² for 450 nm laser^[80]. When the power density is below this threshold, the residual solid product is amorphous carbon with a D peak and a G peak^[81]. Once the power density exceeds this threshold, a sharp decrease in N and O content and a significant increase in C content for the residual solid product can be found by elemental analysis^[29]. The significant increase in the carbon content of the solid product leads to the transition of insulating material to conductive LIG^[75,82] [[Figure 2C](#)].

Reactive molecular dynamics demonstrate that a critical temperature of 2700 K is a prerequisite for the formation of the LIG^[72]. At 2700 K, polyimide molecules can decompose into hexagon rings even in the absence of a metal catalyst, while carbonization products below this temperature are mainly in the form of amorphous carbon chains [[Figure 2D](#)]. In the formation process of LIG, the O and N atoms serve to connect carbon rings, thus accelerating the formation of hexagon rings. In addition to temperature, other parameters also have great effects on the formation of LIG, including heat preservation time, heating and cooling rates, and processing cycles. The heat preservation time and processing cycles affect the formation of LIG [[Figure 2E](#)], while the heating and cooling rates have little effect on the quality of LIG, which is consistent with the experimental results^[83].

PREPARATION AND PROPERTY MODULATION OF LIG

Diversity of laser sources

According to the wavelength, laser sources that have been employed to prepare LIG can be classified into three categories: infrared laser, visible laser, and ultraviolet (UV) laser. Compared to the traditional infrared laser, the UV laser shows two advantages. One is that the LIG prepared by UV laser has higher resolution and better uniformity, which is more conducive to the miniaturization and integration of the devices. The other is that the utilization of UV laser can significantly reduce energy consumption due to the larger absorbance of polymer (e.g., polyimide) to the UV laser^[84].

At the initial stage of LIG study, carbon dioxide laser (pulse duration of ~ 14 μs or continuous wave) is the most common laser source. Due to the large heat-affected zone of the carbon dioxide laser, the linewidth of the fabricated LIG is wide (~ 100 μm)^[85]. Besides, a flexible substrate with a thickness larger than 100 μm is required^[86]. In 2018, Alexandre first reported that a fourfold reduction in ablation depth thickness and a doubled improvement in spatial resolution could be achieved by using a UV laser with a wavelength of 355 nm (pulse duration of 1 μs)^[41]. After that, lasers with other wavelengths were widely used to prepare LIG, including 1064 nm (continuous wave)^[87,88], 532 nm (continuous wave)^[82,89], 450 nm (continuous wave)^[80,90,91], 405 nm (pulse duration of 10~50 ms)^[86,92,93], 355 nm (pulse duration of 10 ps)^[83], 343 nm (pulse duration of 220 fs)^[94,95], and 308 nm (pulse duration of 20 ns)^[96], indicating that the preparation of LIG is independent of laser sources. Compared to laser sources with long pulse widths (continuous wave, millisecond, microsecond, and nanosecond), ultrafast lasers (pulse duration of picosecond and femtosecond) enable higher processing resolution due to the smaller heat-affected zone. The diversity of laser sources promotes the broad application of LIG-based flexible electronic devices.

Diversity of carbon sources

Most carbon-containing materials, including thermoplastic polymers, thermoset polymers, and natural polymers, can be converted into graphene as long as suitable process parameters are applied. As a typical case of thermoplastic polymers, polyimide is the most common carbon source in early research of LIG [Figure 3A and B] due to its unique features in terms of material stability, high-temperature resistance, and flexibility^[97,98]. With the rapid progress of LIG preparation, other common polymeric materials, such as PEEK^[99] [Figure 3C], PDMS^[47,100] [Figure 3D], phenolic resin^[101] [Figure 3E], self-assembled block copolymer and resin composite^[102,103] (such as the Kevlar fiber in Figure 3F), photoresists^[104], PTFE^[105], PES^[106], and resorcinol^[107], have been proven to be possible to fabricate LIG.

For materials with poor properties of carbon formation, previous studies have shown that only low-quality amorphous carbon can be produced under laser irradiation. To solve this problem, Tours has developed multiple irradiations method [Figure 3G] to carbonize these materials into graphene, such as wood^[108,109], potato skins, bread, and cellulose clothing^[110] [Figure 3H]. The adopted defocusing strategy reduces the temperature gradient to avoid the exfoliation of carbonization products, allowing these products to be irradiated repeatedly to improve their quality. The diverse carbon sources open up a new route for recycling waste items (e.g., preparing electronic devices from these waste items). In addition, some low-quality amorphous carbon can be transformed into high-quality graphene by laser irradiation, thus providing a facile method for improving the quality of carbon at a low cost. However, the quality of LIG is much lower compared to graphene prepared by CVD or epitaxially grown. Therefore, more efforts should be devoted to improving the quality of LIG in the future, such as by adopting a catalytic approach.

Property modulation methods of LIG

Effect of process parameters

The method of tuning laser parameters [Figure 4A], including laser power, scanning speed, frequency, and out-of-focus distance, is widely used to modulate the properties of LIG, including the porosity, thickness, and square resistance^[79]. Generally, as the absorbed laser energy increases, the amount of gas produced by the decomposition of the polymer increases, thus resulting in an increase in the hole size of LIG^[111] [Figure 4B]. However, excessive energy destroys the porous structure^[29]. These holes greatly increase the surface area (up to 340 m²/g^[29]) of LIG electrodes, which can help improve device performance in certain fields, i.e., porous electrodes are helpful to improve the performance of supercapacitors by providing sufficient contact between electrode and electrolyte, and plenty of holes increase the reflection ratio of electromagnetic waves to improve electromagnetic shielding effectiveness.

In addition to hole size, the thickness of LIG can also be adjusted by varying laser parameters. The higher the absorbed laser energy, the greater the thickness of LIG^[112]. Although the increase in thickness leads to a decrease in flexibility, thicker electrodes can significantly increase the area-specific capacitance of the supercapacitor and the electromagnetic interference effectiveness of the electromagnetic shielding device. Besides, the increasing laser energy results in a decrease in square resistance^[108] [Figure 4C], which improves the performance of devices that utilize the electrical property of LIG, such as electrothermal actuators and electromagnetic devices. The ratio of I_D/I_G (defect ratio) tends to decrease first and then increase as the absorbed laser energy increases [Figure 4D and E]. This is because the increasing absorbed energy results in the sufficient decomposition of the polymer, while excess energy causes the oxidation of the as-formed LIG in the air.

Effect of processing environments

During polymer carbonization, the oxygen in the processing environment is involved in the process of polymer pyrolysis [Figure 5A], causing the oxidation of the residual solid product. This oxidation not only

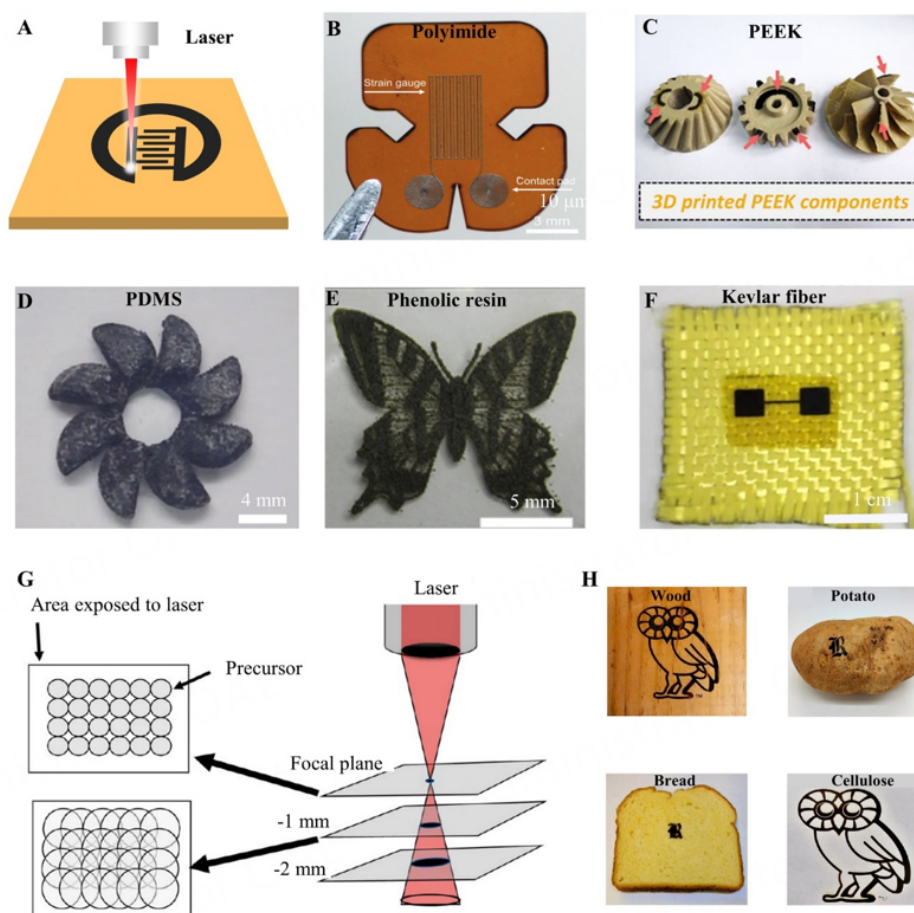


Figure 3. Diversity of the carbon source for LIG. (A) Fabrication of patterned LIG on flexible substrates. (B) Serpentine LIG lines on the polyimide substrate^[41]. Copyright 2018, WILEY-VCH Verlag GmbH & Co. KGaA, Weinheim. (C) Fabrication of patterned LIG on 3D printed PEEK components^[99]. Copyright 2019, American Chemical Society. (D) Preparation of LIG gears on the PDMS substrate^[100]. Copyright 2017, WILEY-VCH Verlag GmbH & Co. KGaA, Weinheim. (E) Preparation of LIG butterflies on the phenolic resin substrate^[101]. Copyright 2018, Elsevier. (F) The LIG pattern on the Kevlar fiber^[102]. Copyright 2022, American Chemical Society. (G) Schematic diagram of multiple repeated irradiations. (H) LIG patterns on wood, potatoes, bread, and cellulose clothing. Reproduced with permission^[10]. Copyright 2018, American Chemical Society.

changes the surface morphology of LIG (e.g., lamellar and striated mesoporous structure for the oxygen-containing environment and layered microporous structure for the oxygen-free environment, as exhibited in [Figure 5B](#)) but also increases the oxygen content in the residual solid product^[113] [[Figure 5C](#)]. Generally, the LIG fabricated in the oxygen-containing processing environment (e.g., air or oxygen environments) shows hydrophilic, while it can be transformed to hydrophobic by changing the processing environment to Ar or H₂^[113]. Different flexible LIG-based electronic devices require different properties of LIG, i.e., hydrophilic LIG is more suitable for supercapacitors and fuel batteries, while hydrophobicity is necessary for actuators, sensors, electromagnetic devices, and nanogenerators. These variable features allow more possibilities for the practical application of LIG.

Although LIG shows hydrophilic in oxygen-containing processing environments, the oxidation effect of the as-formed LIG at high temperatures results in a decrease in the electrical property. For example, a 5-fold reduction in square resistance can be found by changing the processing environment from air to Ar at a fixed laser power^[86] [[Figure 5D](#)]. In the inert gas environment, the oxidation of the as-formed LIG is

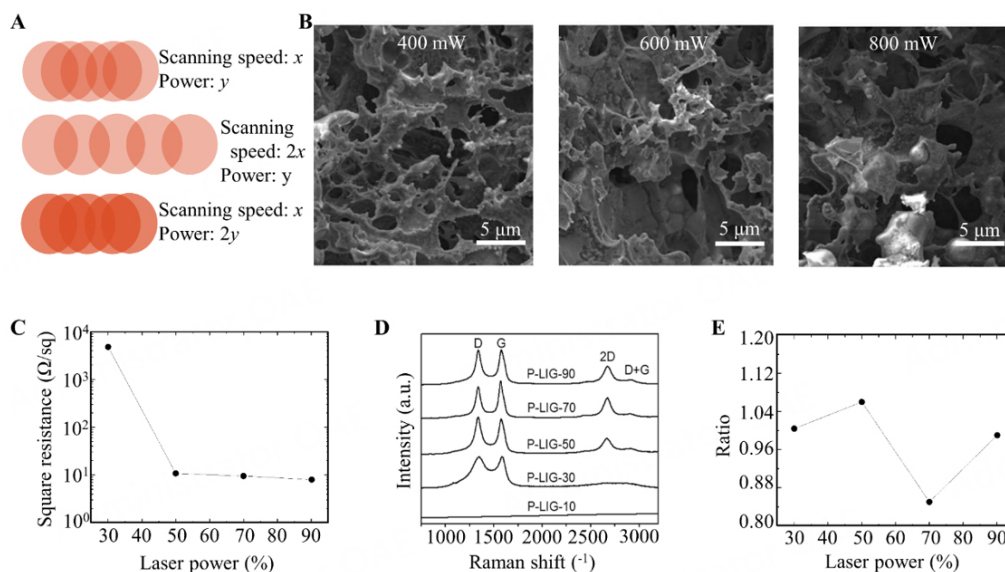


Figure 4. Effect of process parameters. (A) Effects of the laser power and scanning speed. Reproduced with permission^[79]. Copyright 2018, Elsevier. (B) Morphology of LIG at different powers of 400 mW, 600 mW, and 800 mW. Reproduced with permission^[111]. Copyright 2019, The Author(s), published by Applied Physics Letters. (C) Correlation of square resistance of LIG with laser power. (D) Raman spectra at different powers. (E) Variation of the ratio of I_D/I_G at different powers. Reproduced with permission^[108]. Copyright 2017, WILEY-VCH Verlag GmbH & Co. KGaA, Weinheim.

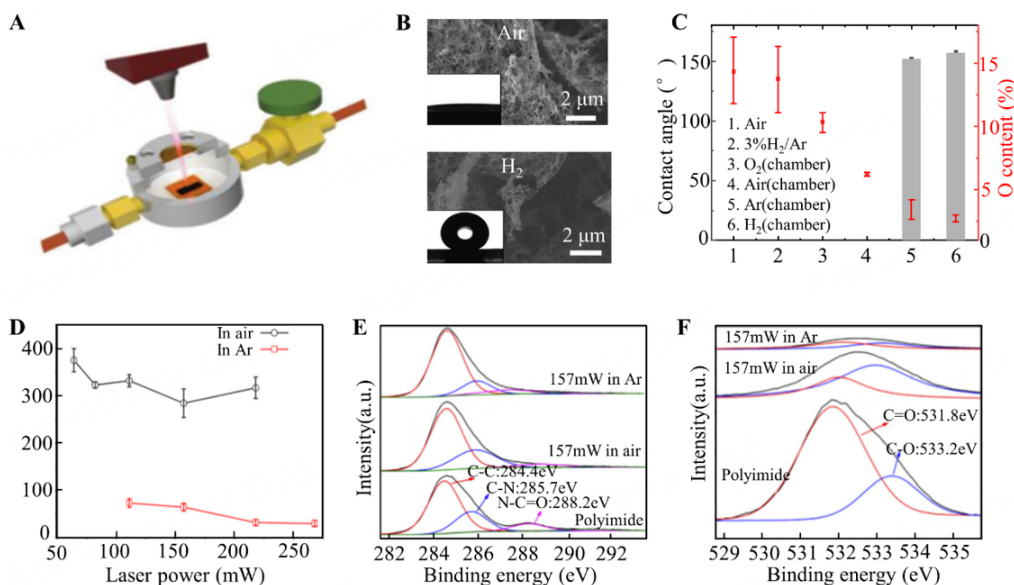


Figure 5. Effect of processing environments. (A) Schematic diagram of the device for different processing environments. (B) Surface morphology of LIG fabricated in different processing environments of air and H_2 . (C) The contact angle and O content in different processing environments. Reproduced with permission^[113]. Copyright 2017, WILEY-VCH Verlag GmbH & Co. KGaA, Weinheim. (D) Correlations of square resistance with laser power for different processing environments. (E) XPS C1s peak of polyimide and LIG in air and Ar environments. (F) XPS O1s peak of polyimide and LIG in air and Ar environments. Reproduced with permission^[86]. Copyright 2016, Elsevier.

suppressed, thus resulting in fewer impurities of LIG [Figure 5E and F]. However, this processing environment causes LIG to show hydrophobic features, which is unfavorable for supercapacitors or fuel batteries^[86]. Combining with post-treatment methods, such as the air or oxygen plasma treatment^[114,115], the

hydrophobic electrode can become hydrophilic while the resistance of LIG remains unchanged, achieving compatibility between hydrophilic and high electrical properties.

Effect of heteroatom doping

Despite large amounts of defects in LIG, these defects are favorable to heteroatom doping (e.g., conductive ink, functional elements, and metal nanoparticles), which is an effective method to adjust LIG properties. From the perspective of engineering application, the adjustable features of LIG are helpful in broadening its applications. To date, various heteroatom doping methods, including pre-treatment of carbon sources and post-treatment of LIG, have been widely used to modulate the property of LIG (e.g., hydrophilic/hydrophobic and electrical/electrochemical properties)^[52].

Pre-treatment means adding other materials into carbon sources before carbonization, which is usually bulk doping. Depending on the added material, it can be used to modulate the hydrophilic/hydrophobic and electrical/electrochemical properties of LIG. For the added materials of certain functional elements (e.g., fluorine element), the hydrophilic LIG can be converted to hydrophobic. For example, Chen *et al.* proposed a one-step method for the preparation of F-doped LIG via interface ablation^[116] [Figure 6A]. During this process, the high temperature generated by the laser causes the decomposed F atoms to be doped into LIG in one step, thus enabling the hydrophobic LIG [Figure 6B]^[116]. For the added materials of metal nanoparticles, its incorporation can effectively improve the electrical/electrochemical properties of LIG. As a typical example, Han *et al.* proposed a laser direct writing method to synthesize composite metal particles (e.g., Cu, Co, Ni, Fe, NiFe)/LIG electrodes in one step^[117]. Before laser irradiation, the carbon source of the cedar is immersed in a metal salt precursor. Under the high-temperature conditions generated by the laser, the metal ions are reduced and attached to the surface of LIG, resulting in improved electrical/electrochemical properties^[117]. In addition to metal particles, low-dimensional nanomaterials (e.g., MoS₂^[118], ZnO^[119]) have also been widely used due to their high surface area. Using a similar method, Deng *et al.* synthesized composite MoS₂/carbon electrodes in one step from these inexpensive materials of citric acid (C₆H₈O₇), ammonium molybdate tetrahydrate ((NH₄)₆Mo₇O₂₄·4H₂O) and sodium sulfide (Na₂S)^[118]. The simultaneous formation of MoS₂ NPs and LIG simplifies the preparation process. The synergistic effect of the large number of catalytically active sites exposed in the MoS₂ nanoparticles and the carbon materials allows the composite electrode to exhibit excellent catalytic performance and stability for hydrogen precipitation reactions in acidic solutions [Figure 6C]^[118].

After the formation of LIG, its properties (e.g., hydrophilic/hydrophobic and electrical/electrochemical properties) can also be tuned by the post-treatment method, which includes surface and bulk doping. Plasma treatment (e.g., fluorine plasma, oxygen plasma, and air plasma) is a convenient surface post-treatment method to adjust the hydrophilic/hydrophobic property of LIG. Generally, the post-treatment of LIG by fluorine plasma is helpful to hydrophobicity, while the oxygen/air plasma contributes to hydrophilicity. Besides, electroless plating is also a surface post-treatment method to adjust the electrical/electrochemical property of LIG. The deposition materials mainly contain metal nanoparticles^[120] (e.g., Ni nanoparticles) and low-dimensional nanomaterials^[121] (e.g., ZnO nanoparticles). As a typical example, Zhu *et al.* prepared a high-sensitive biosensor (3500 μA mM⁻¹ cm⁻² for glucose detection in a wide range of 0-30 mM) by electroless plating of Ni and Au on the surface of LIG^[122]. The incorporation of metal nanoparticles contributes to increasing the specific surface area and lowering the charge transfer resistance. Apart from the above surface post-treatment method, the bulk post-treatment method has also been widely investigated to adjust the electrical/electrochemical property of LIG. The holes of LIG can be used to fill with other materials to fabricate composite electrodes. For example, Zhang *et al.* fabricated composite electrodes with excellent electrochemical property (areal capacitance of 1425 F/g at 1A/g) by filling porous

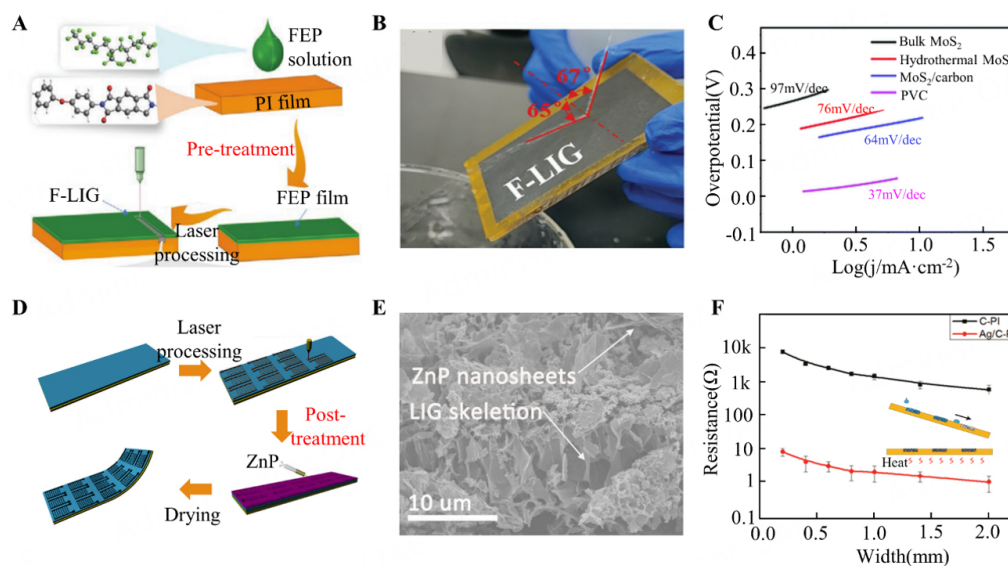


Figure 6. Effect of heteroatom doping. (A) Fabrication process of F-doped LIG by pre-treatment method. (B) Photograph of contact angle of F-doped LIG. Reproduced with permission^[116]. Copyright 2021, WILEY-VCH Verlag GmbH & Co. KGaA, Weinheim. (C) Comparison of electrochemical properties for different electrodes. Reproduced with permission^[118]. Copyright 2016, The Royal Society of Chemistry. (D) Post-treatment of LIG with the incorporation of ZnP. (E) Distribution of ZnP on the surface of LIG. Reproduced with permission^[43]. Copyright 2021, Elsevier. (F) Correlations of resistance with width for LIG and Ag-doped LIG. Reproduced with permission^[123]. Copyright 2016, American Chemical Society.

LIG with ZnP nanosheets^[43] [Figure 6D and E], which mainly benefits from the fact that the hydrophilic LIG can easily capture the ZnP solution and porous structure can store large amounts of ZnP solution. The doped ZnP improves the adsorption energy of electrolyte ions and reduces the band gap^[43]. In addition, the conductive ink can be selected to fabricate high-conductive LIG. Rahimi *et al.* achieved a 2500-fold improvement in the electrical property by filling porous LIG with conductive silver ink [Figure 6F]^[123]. Except for the silver ink, other conductive inks (e.g., copper ink^[124], nickel ink^[125], and CNT ink^[126]) are also possible.

LIG-BASED FLEXIBLE ELECTRONIC DEVICES

As discussed above, various laser and carbon sources can be used for the fabrication of LIG. Besides, the property of LIG can be easily modulated by diverse approaches. From the perspective of device preparation, these advantages promote many possibilities of LIG for flexible electronic devices. In this section, a comprehensive review of various LIG-based flexible electronics is presented.

Actuators

Facilitated by the good flexibility, optical property (high absorption of 99% for wavelengths from 280 nm to 2500 nm^[127]), thermal stability (> 900 °C^[52]), and electrical property (conductivity of 5-25 S/cm^[29]) of LIG, graphene-based actuators have witnessed great development in the past 8 years. Responsive mechanical motions (e.g., shape and structure variation) of actuators under various external environmental stimuli (e.g., electricity, heat, light, magnetism, humidity, solvents, and pH) play a crucial role in many fields, such as energy generators^[128] and soft robots^[129]. The applications of LIG in actuators can be classified into two categories: the electrothermal actuator and the photothermal actuator.

Taking advantage of the excellent and tunable electrical property of LIG, the actuator based on the electrothermal effect has been widely studied. Figure 7A shows the preparation process of the LIG-based

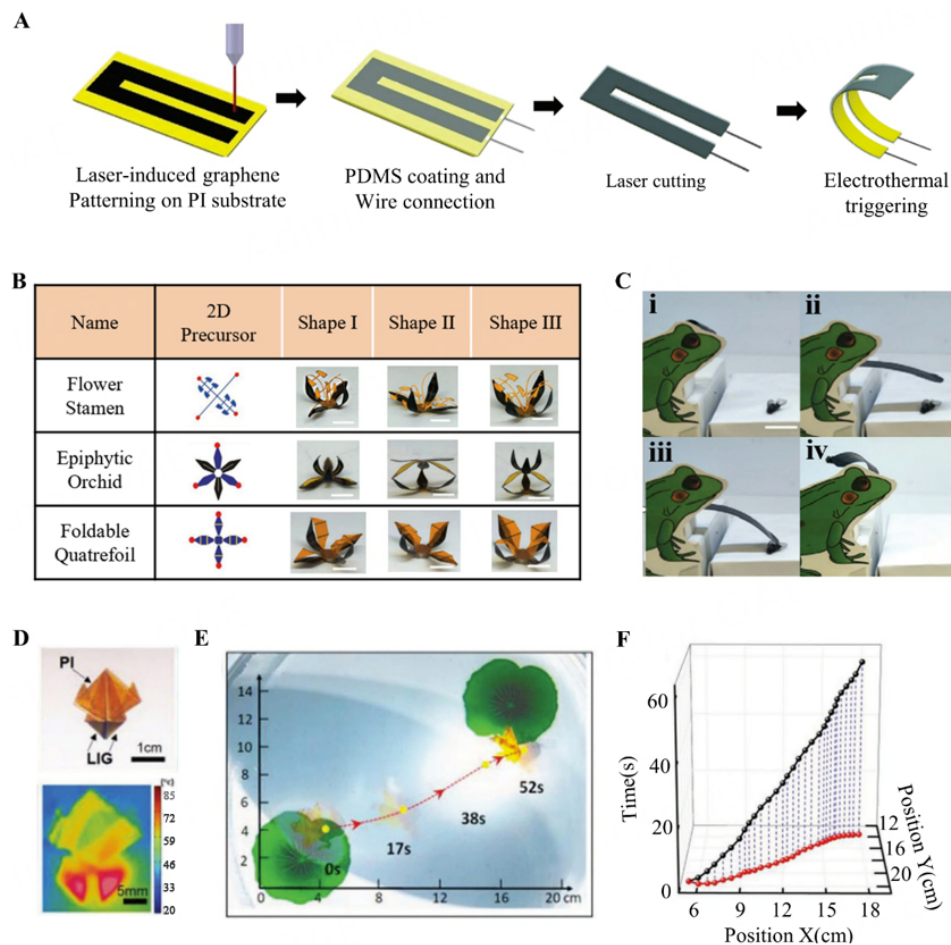


Figure 7. Design of actuator based on LIG. (A) Preparation process of U-type electrothermal actuator. (B) Design of 2D precursor and fixed nodes for flower stamen, epiphytic orchid, and foldable quatrefoil. (C) Photographs of bionic frog tongue grasping insects on the table. Reproduced with permission^[130]. Copyright 2020, WILEY-VCH Verlag GmbH & Co. KGaA, Weinheim. (D) Photograph of a 3D frog and its temperature distribution under light illumination. (E), Positions of a 3D frog at different times. (F) The movement path of the 3D frog under light illumination. Reproduced with permission^[131]. Copyright 2021, WILEY-VCH Verlag GmbH & Co. KGaA, Weinheim.

electrothermal actuator: (1) LIG is first prepared on the polymer substrate; (2) a layer of PDMS is then coated for encapsulation; (3) the excess area is next tailored by the method of laser cutting; and (4) an electrothermal actuator is finally obtained^[130]. Under different voltages, the electrothermal actuator bends to different angles (0~1080°). By fixing nodes, some complex shapes of the electrothermal actuator can be realized, such as flower stamen, epiphytic orchid, and foldable quatrefoil, by varying the shape of LIG and fixed nodes. Particularly, three different shapes of electrothermal actuators can be realized by controlling the voltage for the same 2D precursor [Figure 7B]. These features illustrate the great potential of electrothermal actuators in various applications, such as bionic electronic devices. As shown in Figure 7C, the bionic frog tongue can repeatedly and effectively grab the insects on the table. Especially the response time and recovery time are within 5 seconds (the fastest response time currently reported) due to the excellent electrical property and thermal conductivity^[130]. However, the response time can be further improved by increasing the electrical property of LIG, which has rarely been explored in the current research. For certain occasions, fast response time is important. For instance, for soft gripping robots, fast response time is beneficial to improve efficiency.

After laser illumination, LIG has a high absorption of 99% for the light with a wavelength from 280 nm to 2500 nm, thus enabling it to be an ideal material for the fabrication of the photothermal actuator^[127]. Recently, using the methods of laser cutting and laser carbonization, Wang *et al.* fabricated planar photothermal actuators on the PDMS substrate^[100]. Due to the different absorbances of PDMS and LIG, the temperatures of PDMS and LIG are different under the same light illumination. By designing a suitable LIG shape on the gear, the rotation of the gear can be achieved under light illumination due to the difference in surface tension between the LIG and PDMS sides^[100]. Combined with origami craft, a 3D frog with its head carbonized can be fabricated [Figure 7D]. The temperature of its head is higher than other positions under light illumination, which drives the 3D frog to move [Figure 7E and F]. By changing the carbonized position of bionic frogs, different movement paths can be realized^[131]. Increasing the power density or decreasing the scanning speed is favorable to the improvement of the absorbance of LIG, thus improving the response time. To date, the reported response time is 0.48 ± 0.14 s with a velocity of 11.05 ± 0.87 mm/s^[127]. Compared to electrothermal actuators, photothermal actuators can be operated in energy-saving mode by sunlight exposure, which is suitable for energy generators.

Sensors

Compared to traditional sensors (e.g., strain sensor, gas sensor, and pressure sensor) fabricated by lithography technology, LIG-based sensors exhibit several distinct advantages. First, the electrode pattern can be directly prepared on the flexible substrate, thereby simplifying the preparation process and reducing the cost. Second, porous LIG has some unique characteristics, such as enhanced tensile property, excellent gas adsorption/desorption property, and natural piezoresistive property, which are favorable for improving the performance of the device. Third, the patterned electrode can be processed in one step without a mask, which facilitates the low-cost fabrication of LIG-based sensors.

Strain sensor

Compared to traditional metal-based strain sensors, the natural hole of LIG not only improves the flexibility of the electrode but also adjusts the sensitivity of the strain sensor [Figure 8A]. By changing process parameters, the sensitivity can be adjusted from 5.39 to 43.7^[85], which is much larger than the commercial copper-based strain sensors with a sensitivity of 2. Besides, the substrate also has great effects on the sensitivity (e.g., the sensitivity of 10,000 at 100% strain for PDMS substrate^[132] [Figure 8B] and sensitivity of 43.7 at 1.5% strain for polyimide substrate^[85]). In the past decade, various applications of LIG-based strain sensors have been widely explored, which range from equipment state detection and human health monitoring. For equipment state measurement, polyimide substrate is more suitable due to its stability^[133]. As for the wearable sensor, the soft substrate is more suitable due to its better conformability.

As an example of the equipment state measurement, Yu *et al.* applied ultra-thin LIG-based strain sensors to the deformation measurement (e.g., bending, twisting, and impact) of morphing aircraft^[96] [Figure 8C]. The sensitivity of the LIG-based strain sensor is 30 times higher than that of commercial strain sensors, which helps to improve the measurement accuracy. As illustrated in Figure 8D and E, the resistance variation of strain sensors is linearly related to the bending and twisting angle. When a morphing aircraft is impacted by an object, the local area at the impact position will be deformed, thus resulting in the resistance variation of the strain sensor in the corresponding area^[96]. In addition to morphing aircraft, LIG-based strain sensors can also be used in other devices, such as gesture monitoring for robots^[46]. The linear range of LIG-based strain sensors with polyimide substrate is ~2%, beyond which the deformation of polyimide enters into the plastic stage. This feature limits its further application in the equipment state measurement with large strain.

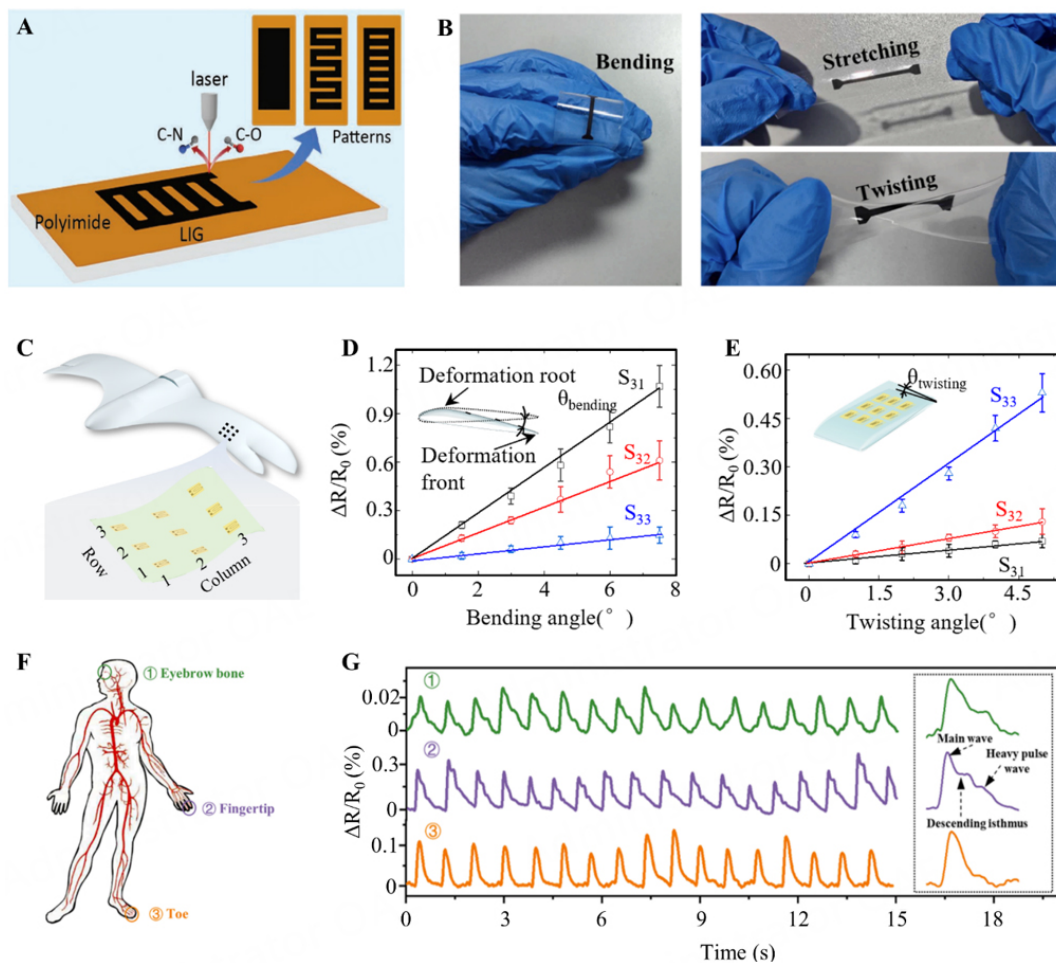


Figure 8. Design of LIG-based strain sensor. (A) Schematic diagram of LIG-based strain sensor with the polyimide substrate^[133]. Copyright 2019, WILEY-VCH Verlag GmbH & Co. KGaA, Weinheim. (B) Photographs of LIG-based strain sensors with the PDMS substrate in different deformation states (e.g., bending, stretching, and twisting)^[135]. Copyright 2022, Elsevier. (C) Schematic diagram of LIG-based strain sensor in morphing aircraft. (D) The $\Delta R/R_0$ versus strain for different bending angles. (E) The $\Delta R/R_0$ versus strain for different twisting angles^[96]. Copyright 2022, WILEY-VCH Verlag GmbH & Co. KGaA, Weinheim. (F) LIG-based strain sensor attached to different positions. (G) Resistance variation rate of strain sensor attached to three positions in humans^[135]. Copyright 2022, Elsevier.

Since the first discovery of LIG, the application of LIG-based strain sensors for human health monitoring has been a hot direction. In this field, porous electrodes are beneficial for improving comfortability and reducing the risk of skin inflammation. Employing this feature, various wearable sensors have been developed, such as gas-permeable sensors for the detection of ECG signals^[134]. In addition, high-sensitive strain sensors for other physiological signals can also be fabricated. As a typical case, Chen *et al.* prepared hydrophobic strain sensors (sensitivity of 2212.5, response time of 0.11 s, and ultralow detection limit of 0.0167% strain) with the substrate of PDMS^[135]. This sensor can detect not only the pulse wave (three peaks of P, T, and D), but also subtle signals in humans (e.g., eyebrow bone, fingertip, and toe tip waves in Figure 8F). As seen in Figure 8G, three feature peaks are repeatedly detected at these three positions^[135]. The strain of LIG on the PDMS substrate can reach 100% without extra structure design^[132]. Thanks to these favorable features, it is expected to be an important electrode option for future wearable electronics.

Gas sensor

LIG is a promising material for gas detection due to its huge surface area ($320 \text{ m}^2/\text{g}^{[52]}$), which contributes to the strong interaction with the gas. In this interaction, the absorption and desorption of the gas contribute to the convective heat exchange, causing the resistance variation of LIG^[136] [Figure 9A]. In particular, the resistance variation is dissimilar for various gases due to the different thermal conductivities of the gases. Employing these advantages, various gas sensors for environmental monitoring and gas leakage detection have been studied in the past decade^[137]. As exhibited in Figure 9B, a gas sensor was fabricated to detect hazardous gases, such as NO_2 ^[102,138]. On this basis, Stanford *et al.* optimized the above structure, which is composed of LIG wire with large resistance and LIG electrode with small resistance^[139] [Figure 9C]. In this structure, the heat is mainly concentrated at the location of the LIG wire, which is helpful for the improvement of sensitivity. This sensor can detect various gases, including oxygen, air, and helium, and has good stability in sensitivity over multiple cycles^[139] [Figure 9D]. By adjusting process parameters, the hole size and sensitivity can also be modulated. Besides, LIG method allows the preparation of sensors on different flexible substrates, such as polyimide, PDMS^[138], and textile^[102], thus significantly broadening application ranges. These resistive gas sensors are suitable for most gases (e.g. toxic, combustible, and inert gases). However, the sensitivity is small for gases with poor thermal conductivity [e.g., Ar with a thermal conductivity of $25 \text{ mW}/(\text{m}\cdot\text{K})$]. Besides, it is not possible to distinguish between gases with close thermal conductivity (e.g., oxygen, air, and N_2).

In addition to resistive gas sensors, another type of electrochemical gas sensor has been developed in recent years, which converts chemical energy into electrical energy. This type of gas sensor is only suitable for gases that can undergo redox reactions. As a typical example, Dosi *et al.* demonstrated that the LIG-based electrochemical sensor can be used to detect methane, ethane, and propane^[140]. For alkane gases, the electrochemical signal varies greatly due to electro-oxidation reactions. Due to the differences in the reaction rates for different alkane gases, the electrochemical signal is varied. Based on this mechanism, the capacitive gas sensor is another option for gas detection. As illustrated in Figure 9E, methane and oxygen are electro-oxidized to carbon dioxide and water under the catalytic effect of Pd nanoparticles, resulting in the variation of current. This current is linearly related to the concentration of methane, ethane, and propane^[140]. Compared to currents in three gas conditions [Figure 9F], it can be found that the sensitivity of methane is the highest due to its fastest oxidation reactions. The sensitivity of methane decreases in humid conditions, mainly because water reduces the reaction rate. Therefore, the hydrophobic property is necessary for the stable performance of the devices. Besides, the performance of the gas sensing can be further improved by enhancing the electrochemical property of LIG. Compared to resistive gas sensors, electrochemical gas sensors can distinguish gases with close thermal conductivity (e.g., ethane and propane). However, they are not suitable for the detection of common gases (e.g., NO_2 , N_2 , and He).

Pressure sensor

When subjected to pressure, the decrease in hole spacing leads to a decrease in the resistance of LIG^[89,141] [Figure 10A], showing a different principle from that of traditional piezoelectric sensors^[142]. Table 1 illustrates the performance comparison of LIG-based pressure sensors with others^[143-149]. As can be seen, there are three advantages of LIG-based pressure sensors. Firstly, LIG can be directly used as sensing material, simplifying the multilayer structure of the traditional piezoresistive sensor. Secondly, despite the lower sensitivity of the LIG-based pressure sensor, it shows a larger linear range (e.g., 10-100 kPa in Figure 10B). Thirdly, LIG is embedded in the substrate, which avoids interface mismatch between the metal electrode and the substrate. Thanks to these features, various LIG-based pressure sensors have emerged in recent years for different applications.

Table 1. Performance comparison of LIG-based pressure sensors with others

Sensing mode	Materials	Sensitivity (kPa ⁻¹)	Linear range (Pa)	Ref.
Resistive	LIG/ecoflex	1.28	2-800	[89]
Resistive	LIG/PDMS	0.00123	10-100 k	[141]
Resistive	LIG/ cardboard	0.563	10-50 k	[143]
Resistive	PI/Mxene/silver/paper	509.5	0.5-10 k	[144]
Resistive	SWNT/PDMS	1.8	0.6-200	[145]
Resistive	Au-coated paper/PDMS	1.14	13-5000	[146]
Resistive	Carbonized silk nanofiber membrane/PDMS	34.47	100-400	[147]
Capacitive	rGO/SiO ₂ /PEN	40.8	39-630	[148]
Capacitive	LIG/PDMS	2.6	-	[149]

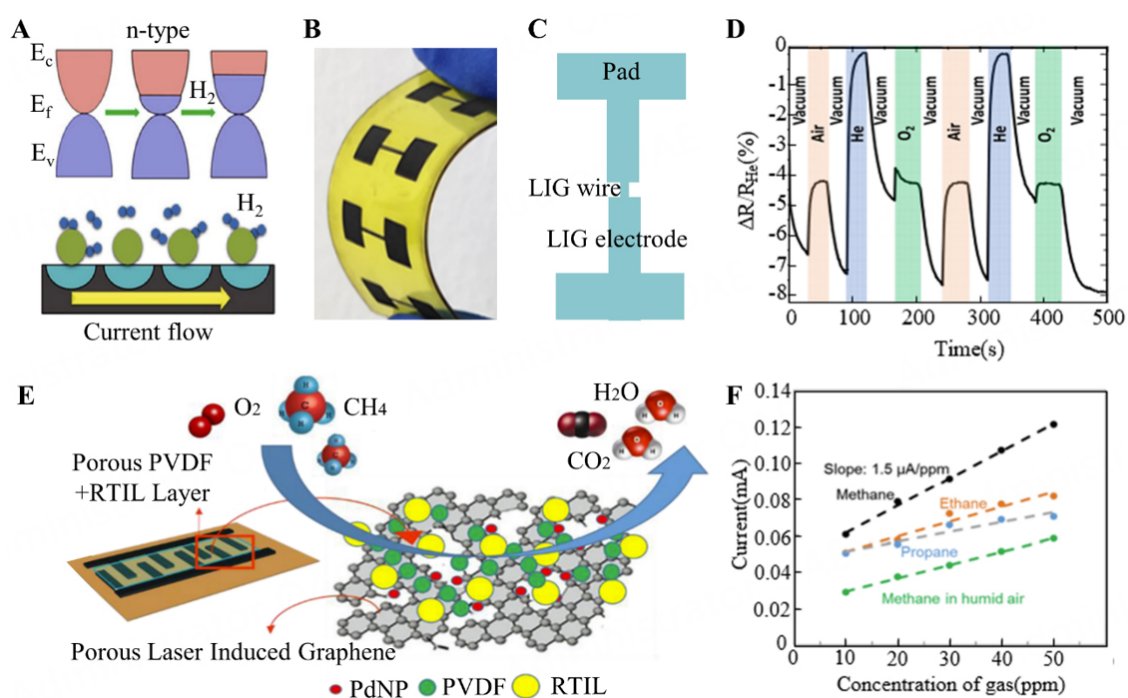


Figure 9. Design of LIG-based gas sensor. (A) Mechanism of resistive sensors for gas detection. Reproduced with permission^[136]. Copyright 2019, American Chemical Society. (B) Photograph of the resistive gas sensor^[102]. Copyright 2020, American Chemical Society. (C) Schematic diagram of the resistive gas sensor with optimized structure. (D) Cyclic test of the resistive gas sensor in the environments of vacuum, air, and helium^[139]. Copyright 2019, American Chemical Society. (E) Mechanism of electrochemical gas sensors for the detection of methane. (F) Correlation of the current with the gas concentration for methane, ethane, propane, and methane in the humid air. Reproduced with permission^[140]. Copyright 2019, American Chemical Society.

Traditional electronic skin can only monitor physiological signals but cannot independently perform alarms. Utilizing the above effect, Chen *et al.* fabricated a dual-functional electronic skin that consists of health monitoring and self-alarm^[133]. When the LIG-based sensor is placed on the mask near the nose, the regular breathing of the human causes the LIG electrode to be subjected to periodic pressure, thus resulting in the periodic variation of the resistance. Meantime, the generated Joule heat results in the expansion of the surrounding air when a voltage is applied, thus generating sound waves. As shown in Figure 10C, the resistance shows periodic variation for normal breathing, and the sound pressure is within the normal range. Once the respiratory pause exceeds 10 seconds, sound pressure increases sharply, thus raising an

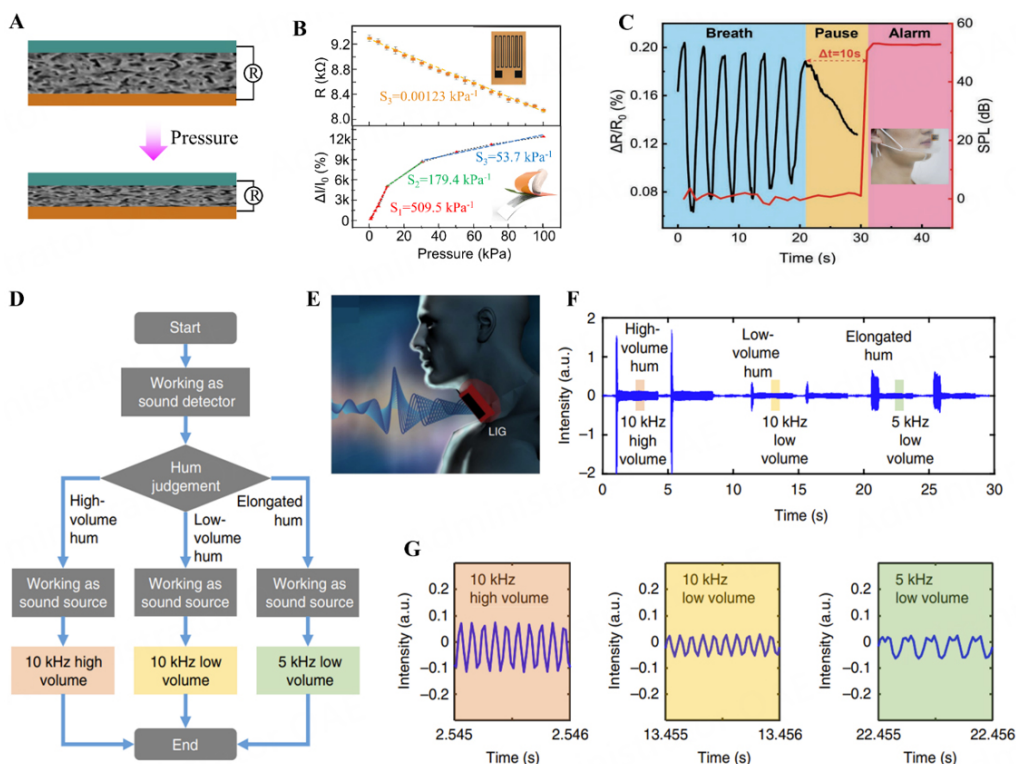


Figure 10. Design of LIG-based pressure sensor. (A) Schematic diagram of the piezoresistive principle of LIG. Reproduced with permission^[141]. Copyright 2020, The Authors. Published by WILEY-VCH Verlag GmbH & Co. KGaA, Weinheim. (B) Comparison of sensitivity and linear range of LIG-based pressure sensors^[141] (Copyright 2020, The Authors. Published by WILEY-VCH Verlag GmbH & Co. KGaA, Weinheim) and traditional piezoresistive sensors^[144] (Copyright 2021, American Chemical Society). (C) Resistance variation and sound pressure of LIG-based sensor. Reproduced with permission^[133]. Copyright 2019, WILEY-VCH Verlag GmbH & Co. KGaA, Weinheim. (D) Working Principle of the artificial throat. (E) Photograph of the artificial throat. (F) Different types of hums are detected and transformed by the intelligent artificial throat. (G) The magnified diagram of the transformed sound. Reproduced with permission^[150]. Copyright 2017, The Author(s), published by Nature.

alarm^[133]. The unique feature of sound pressure grants the traditional electronic skin an important alarm function with no extra costs. In the future, more efforts are worthwhile to further explore the potential applications of this unique feature in electronic skin.

In addition, this feature is also used in the fabrication of acoustic devices, such as artificial throats. As a typical example, Tao *et al.* prepared an intelligent artificial throat that integrates sound generation and sound detection in a single device via laser-carbonizing polyimide^[150]. For sound generation, the results show that the artificial throat can emit a broad-spectrum sound from 100 Hz-40 kHz due to the high thermal conductivity and low thermal capacitance of LIG. As for sound detection, the porous structure of LIG is extremely sensitive to the weak vibration of the throat. On this basis, they combined the device with a neural network approach [Figure 10D] to transform different volumes, frequencies, and durations of hum, scream, or cough sounds into sounds with special meanings. The artificial throat can not only recognize different tones but also decode different types of expressions from mute people, allowing them to speak rich sentences^[150] [Figure 10E-G]. This application opens up a new application of LIG-based flexible devices in the wearable field, which is expected to have a significant impact in the fields of biomedicine and voice recognition. For wearable acoustic devices, the choice of soft materials (e.g., PDMS and Ecoflex) as carbon sources can effectively improve the conformability of electronic devices. As for the performance of the device, it should be investigated in future studies.

Electromagnetic devices

Although defects in LIG affect the electrical conductivity, these defects aggravate the polarization loss and help to improve the electromagnetic interference performance (EMI). Meanwhile, the electrical conductivity of LIG can be improved by heteroatom doping. Therefore, LIG is considered to be an excellent electromagnetic material. According to the application fields of LIG-based electromagnetic devices, they can be divided into radiofrequency antenna devices, electromagnetic shielding devices, terahertz wave modulators, and terahertz imaging devices.

Radiofrequency antennas (e.g., coil antennas, dipole antennas, and microstrip antennas) are key electronic devices in wireless technology, which have been widely used in energy harvesting and wireless communication [Figure 11A]^[151,152]. Generally, the electrical property of LIG cannot be used for antennas. However, the modified LIG (e.g., Ag-doped LIG) effectively solves this problem. As a typical example, Zhu *et al.* adopted Ag-doped LIG to prepare stretchable dipole antennas for wireless transmission^[153]. Meanwhile, a rectenna that continuously harvests energy from external RF sources (e.g., 5G, microwave oven, and Wi-Fi) can be prepared by connecting the dipole antenna and rectifying circuit. Silicone substrate allows arbitrary deformation of a dipole antenna, such as stretching, bending, and twisting in Figure 11B. Significantly, the radiation property of the serpentine dipole antenna is independent of deformation (e.g., bending and twisting in Figure 11C)^[153], which is important for wearable radiofrequency antennas. LIG-based antennas with large fracture strain and simple fabrication procedures show similar performance to traditional metal-based antennas^[154], thus greatly facilitating the great development of wearable radiofrequency antennas.

The randomly distributed holes increase their absorption of electromagnetic waves by multiple reflections of electromagnetic waves [Figure 11D], thus enabling LIG to be an excellent electromagnetic shielding material. As a typical example of electromagnetic shielding devices, Zang *et al.* prepared porous composites of Mo/LIG on fibrous filter paper. By laser irradiating both sides of the film, EMI shielding effectiveness is doubled^[155]. Besides, improving the electrical property of LIG also enhances the performance of the device. Yin *et al.* deposited nickel nanoparticles on the surface of LIG by electrodeposition^[156] [Figure 11E]. As the deposition time increases, the average absorption ratio (ratio of absorbed electromagnetic waves to transmitted electromagnetic waves) increases, while a decrease in absorption ratio occurs by further increasing the deposition time to 50 minutes [Figure 11F]. This is because excess nickel nanoparticles lead to a reduction in impedance matching^[156]. Similarly, other methods (e.g., large power density^[157] and heteroatom doping^[158]) can also be used to enhance the performance of LIG-based electromagnetic shielding devices.

Terahertz is an electromagnetic wave with frequencies ranging from 0.1 THz to 10 THz, which has been widely investigated in recent years due to its great advantages in the fields of communication, environmental monitoring, and medical healthcare^[159]. However, the development of terahertz technology is still in its infancy because of bulky optical modulation elements and the lack of natural materials in this band^[160]. Recent studies have shown that LIG is a potential material for terahertz applications. Wang *et al.* prepared LIG-based terahertz wave modulators^[80] [Figure 11G]. Using the THz focal plane imaging system, they demonstrated that the level of reflected terahertz waves from LIG is comparable to that of a silver mirror in the frequency band of 0.3~0.9 THz, which provides a new approach for the low-cost preparation of terahertz wave modulators^[80]. Despite the great advantages of LIG, there are few reports on the application of LIG in terahertz technology. As a next-generation communication technology, the research on the application of LIG in terahertz fields may be a popular research direction in the following years.

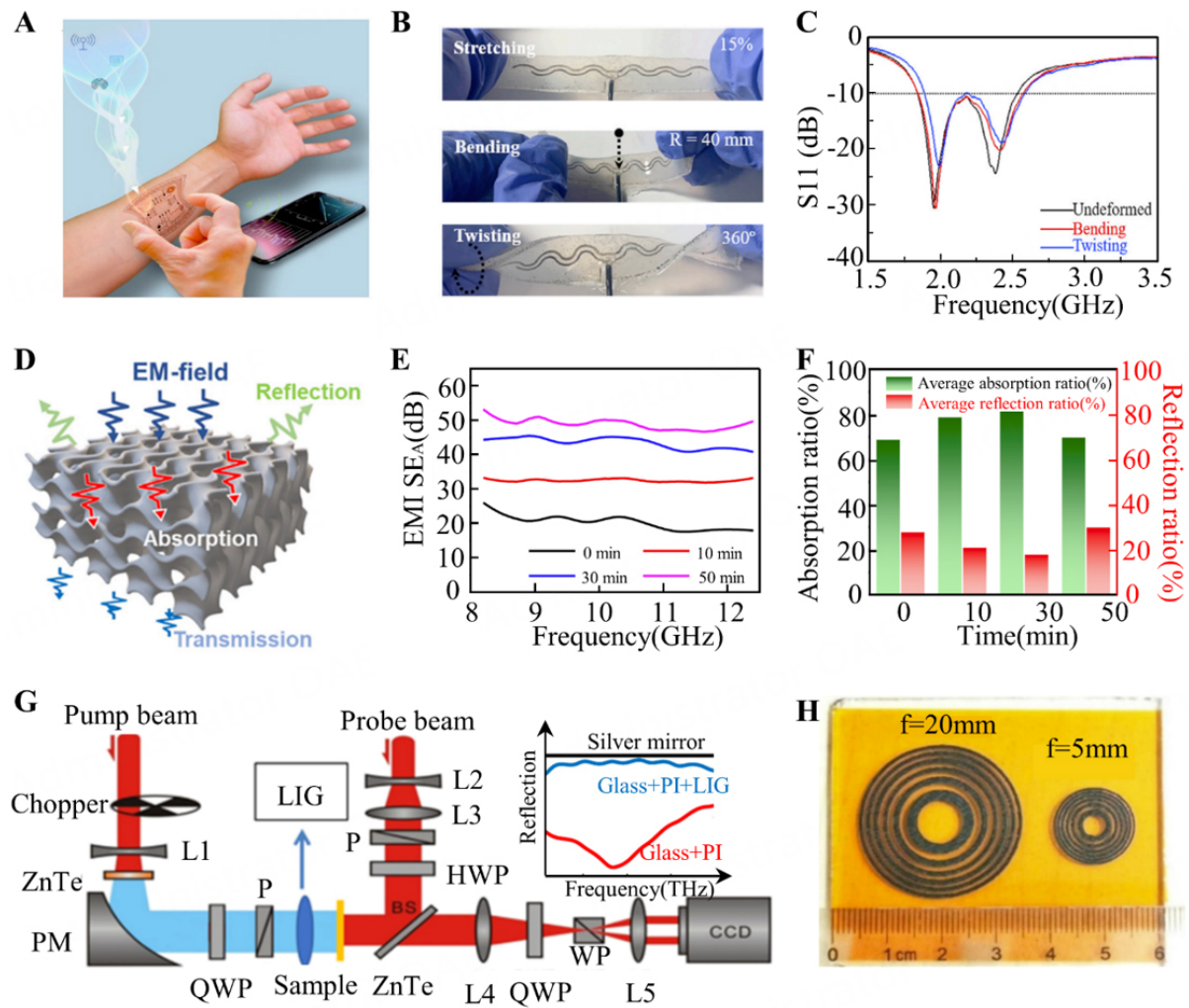


Figure 11. Design of LIG-based electromagnetic devices. (A) Schematic diagram of radiofrequency antennas for wireless communication. (B) Photographs of the stretchable dipole antenna in different deformation states of undeformed, bending and twisting. Reproduced with permission^[153]. Copyright 2021, Elsevier. (C) Variation of S11 in different states of undeformed, bending and twisting. Reproduced with permission^[153]. Copyright 2021, Elsevier. (D) Schematic diagram of electromagnetic shielding of LIG^[155]. Copyright 2020, Elsevier. (E) Variations of EMI shielding efficiency with frequency for different deposition times. (F) Absorption and reflection ratios for different deposition times. Reproduced with permission^[156]. Copyright 2021, Elsevier. (G) Terahertz focal plane imaging system. (H) Photograph of LIG-based Fresnel zone plates with different geometric sizes. Reproduced with permission^[80]. Copyright 2020, Optical Society of America.

In addition to modulators, LIG can also be used for terahertz imaging devices. For example, various Fresnel zone plates with different geometric sizes can be easily fabricated, as shown in Figure 11H. Experimental results show that the focusing effect of the Fresnel zone plate gradually increases as the design focal length decreases. The measured terahertz field distribution agrees well with the measured field-intensity distribution at the focal plane^[80]. This application only shows the great potential of LIG in terahertz imaging devices, including low-cost fabrication, easier pattern process, and excellent imaging results. However, the effect of LIG properties on imaging quality has not been studied. Besides, the effect of carbon sources on imaging quality is also unknown.

Energy storage devices

Nanogenerator

The facile fabrication of LIG electrodes can significantly simplify the preparation process of traditional metal electrodes and reduce the preparation cost. Meanwhile, LIG exhibits excellent electrical properties and good flexibility. Generally, nanogenerators need to withstand thousands of repeated bends, thus resulting in the easy electrode dislodgement of traditional metal-based nanogenerators with poor adhesion between the metal and the flexible substrate^[161]. As for LIG, it is embedded inside the substrate. This special structure effectively avoids the above problem. Taking advantage of these features, LIG is considered to be a promising electrode material for flexible nanogenerators, which can convert mechanical energy into usable electrical energy. According to their working principles, nanogenerators can be classified into triboelectric nanogenerators and hydroelectric nanogenerators.

As a pioneering study, Tour *et al.* fabricated LIG-based triboelectric nanogenerators. [Figure 12A](#) illustrates its working mechanism in detail. When tribo-negative material (e.g., polyimide) comes in contact with tribo-positive material (e.g., aluminum), current flows from LIG to aluminum due to the charge exchange that occurs at the interface. When these two layers are separated, the potential difference will cause the current to flow from aluminum to LIG. The device exhibits excellent performance with an open-circuit voltage greater than 3.5 kV and a peak power greater than 8 mW, which is similar to that of metal-based triboelectric nanogenerators^[162]. In addition to polyimide, other carbon sources (e.g., cork) can also be used to prepare electrodes for triboelectric nanogenerators^[163]. The transfer of LIG to silicone rubber allows the preparation of wearable triboelectric nanogenerators for converting the mechanical energy of human movement (e.g., movement of limbs) into electrical energy^[164]. In addition, other small mechanical energy can also be converted into electricity, such as the movement of water droplets in [Figure 12B](#)^[165]. The facile and low-cost preparation of LIG has greatly promoted the development of triboelectric nanogenerators, which is expected to become the most widely used electrode of triboelectric nanogenerators in the future.

In addition to triboelectric nanogenerators, LIG-based hydroelectric nanogenerators were also developed by utilizing the tunability of the hydrophilic/hydrophobic properties of LIG [[Figure 12C](#)]^[166]. The oxidation degree of LIG is adjusted by controlling the process parameters, thus enabling LIG electrodes with gradual variations in hydrophilic/hydrophobic properties. In humid environments, variation absorptions to the water result in gradient proton distribution, inducing an internal electrical field. As the external relative humidity decreases, the gradient of the proton distribution diminishes. Employing this principle, Huang *et al.* prepared a mask that uses human respiration to generate electricity^[166]. Human inhalation and exhalation cause the nanogenerator to produce regular voltage fluctuations, as shown in [Figure 12D](#)^[166]. This study provides a new scheme for the design of LIG-based nanogenerators, which merits more in-depth study in the future.

Self-powered LIG-based integrated devices that combine nanogenerators and sensors have been a popular research direction of LIG in recent years. In this area, Cheng Huanyu's group has done a lot of exploratory work^[167]. As a typical case, Zhang *et al.* prepared self-powered wearable electronic devices by integrating LIG-based triboelectric nanogenerators, sensors, supercapacitors, and wireless Bluetooth modules^[167] [[Figure 12E](#)]. The triboelectric nanogenerator is used to convert the intermittent mechanical energy of the human into electrical energy stored in a supercapacitor, the sensor is used to monitor the physiological signals of the human, and the Bluetooth module is selected to wirelessly transmit the signals to the interactive interface of mobile terminals (e.g., cell phones). This integrated device can monitor a variety of human physiological signals, such as blood oxygen in [Figure 12F](#) and ECG signals in [Figure 12G](#), exhibiting its great potential for medical health and safety monitoring^[167].

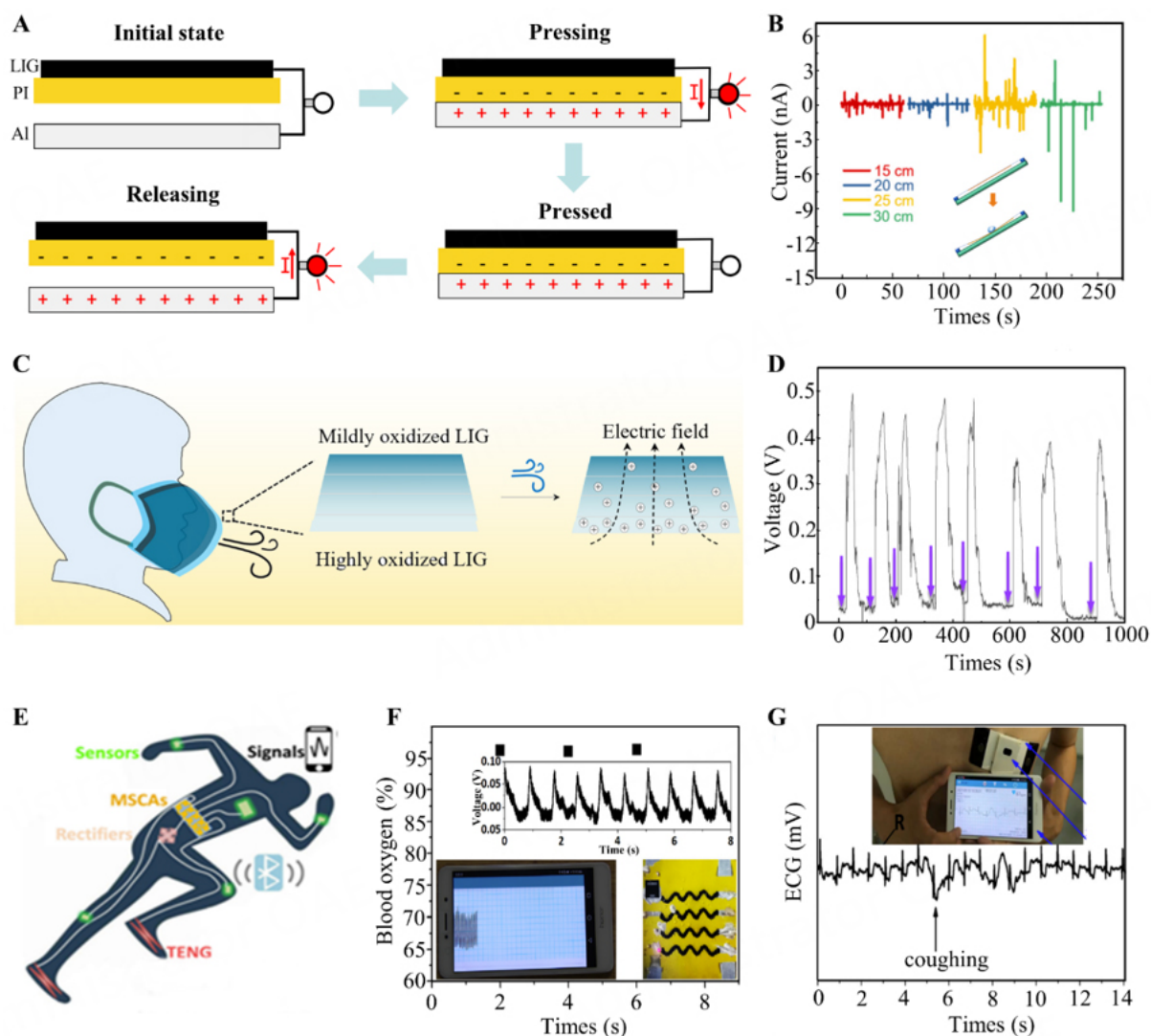


Figure 12. Design of LIG-based nanogenerator. (A) Working mechanism of triboelectric nanogenerator^[163]. Copyright 2019, American Chemical Society. (B) Current generated by drops of water falling at different heights^[165]. Copyright 2022, Elsevier. (C) Working mechanism of hydroelectric nanogenerator. (D) Voltage variations caused by inhalation and exhalation. Reproduced with permission^[166]. Copyright 2020, American Chemical Society. (E) Schematic diagram of LIG-based integrated devices. (F) Blood oxygen detection via self-powered, integrated LIG-based devices. (G) ECG signal detection via self-powered, integrated LIG-based devices. Reproduced with permission^[167]. Copyright 2022, Author(s), published by Applied Physics Reviews.

Supercapacitor

The porous feature of LIG can effectively improve the contact area between electrode and electrolyte, while hydrophilic LIG can make full contact between electrode and electrolyte, thus enabling the improvement of specific capacitance. Besides, diverse approaches can be adopted to further improve specific capacitance, including oxygen-free processing environments^[86] and heteroatom doping^[120,121]. Due to the transferable property of LIG, it can be transferred to silicon rubber to prepare wearable supercapacitors. Facilitated by these features, the research on LIG-based supercapacitors has been a very hot research direction in recent years.

The general preparation process of LIG-based supercapacitors is as follows: (1) a laser is first used to prepare patterned electrodes on the polymer substrate; and (2) an electrolyte is added to complete the fabrication of devices^[168]. The effective operating voltage of supercapacitors is generally around 1 V^[29], which may be different from the operating voltage of daily electronic devices. To solve this issue, the series/parallel schemes of supercapacitor can be adopted [Figure 13A], i.e., the series connection increases the operating voltage [Figure 13B] while the parallel connection is for the improvement of device performance^[43,169] [Figure 13C]. On this basis, Peng *et al.* prepared a flexible solid-state energy storage device with an area-specific capacitance of 9 mF/cm² at a current density of 0.02 mA/cm² by vertically stacking LIG-based supercapacitors^[169]. As proof of practical application, 5 V USB charging can be achieved by connecting five supercapacitors in series^[170] [Figure 13D]. Besides, composite electrodes by heteroatom doping can effectively enhance the performance of LIG-based supercapacitors^[120,121,171]. For instance, Li *et al.* found that the asymmetric flexible supercapacitors with LIG-MnO₂ and LIG-FeOOH possess high specific capacitance and good cycling stability^[171], i.e., the fabricated supercapacitor still has more than 90% capacitance retention after 10,000 bending tests. In addition, the performance of the LIG-based supercapacitor can also be improved by selecting an oxygen-free processing environment^[86].

LIG electrodes can be easily transferred to other substrates. Based on this property, Song *et al.* fabricated a wearable supercapacitor by transferring LIG on polyimide to PDMS^[172] [Figure 13E and F]. The specific capacitance of the wearable supercapacitor maintains over 90% after one thousand times of stretching and twisting cycles^[172] [Figure 13G]. However, LIG is susceptible to external forces during the transfer process, which results in electrode breakage. Another approach is to first prepare LIG as a powder and then pattern it onto the target substrate^[173]. Compared to the first approach, the variety of substrate types is greatly increased from polymers to textiles, but the preparation process is more complicated. The current research on LIG-based supercapacitors has demonstrated the great advantages of LIG. However, the preparation of LIG electrodes on an industrial scale remains a great challenge due to their easy destruction during the preparation process.

In self-powered electronic devices, supercapacitors are generally used as energy storage devices to store the electrical energy generated by energy harvesters. For example, Zhang *et al.* fabricated self-powered stretchable systems, which include stretchable nanogenerators for electricity generation, supercapacitors with high storage energy, and strain sensors for measuring signals^[43] [Figure 13H]. The electricity generated by nanogenerators charges the supercapacitor via a rectifier, which can be significantly increased by connecting multiple supercapacitors in parallel^[43]. In addition, the supercapacitor can be used to store electrical energy generated by other energy harvesters, such as solar panels^[86]. This versatility for energy harvesters has facilitated the large-scale application of LIG-based supercapacitors. Currently, the development of LIG-based integrated systems is still in its infancy. In the future, the potential of LIG-based supercapacitors in self-powered electronic devices is worthy of further exploration.

Battery

In addition, LIG has also found its application in batteries in recent years, including the fuel battery, button battery, and lithium battery^[174,175]. As an application example of the fuel battery, Tours prepared a rechargeable Zn-air battery with metal oxide/LIG composite materials as an electrocatalyst [Figure 14A], which utilizes the hydrophilic property and porous structure of LIG. The composite materials show high activity for oxygen reduction reaction (ORR) and oxygen evolution reaction (OER) in alkaline electrolytes, exceeding the catalytic performance of traditional Pt or RuO₂ in Zn-Air battery. Two zinc-air batteries were connected in series to illuminate the LED [Figure 14B]. Besides, the fuel battery has good stability due to the excellent ORR/OER activity of the fabricated LIG electrocatalyst^[176] [Figure 14C]. Other materials (e.g.,

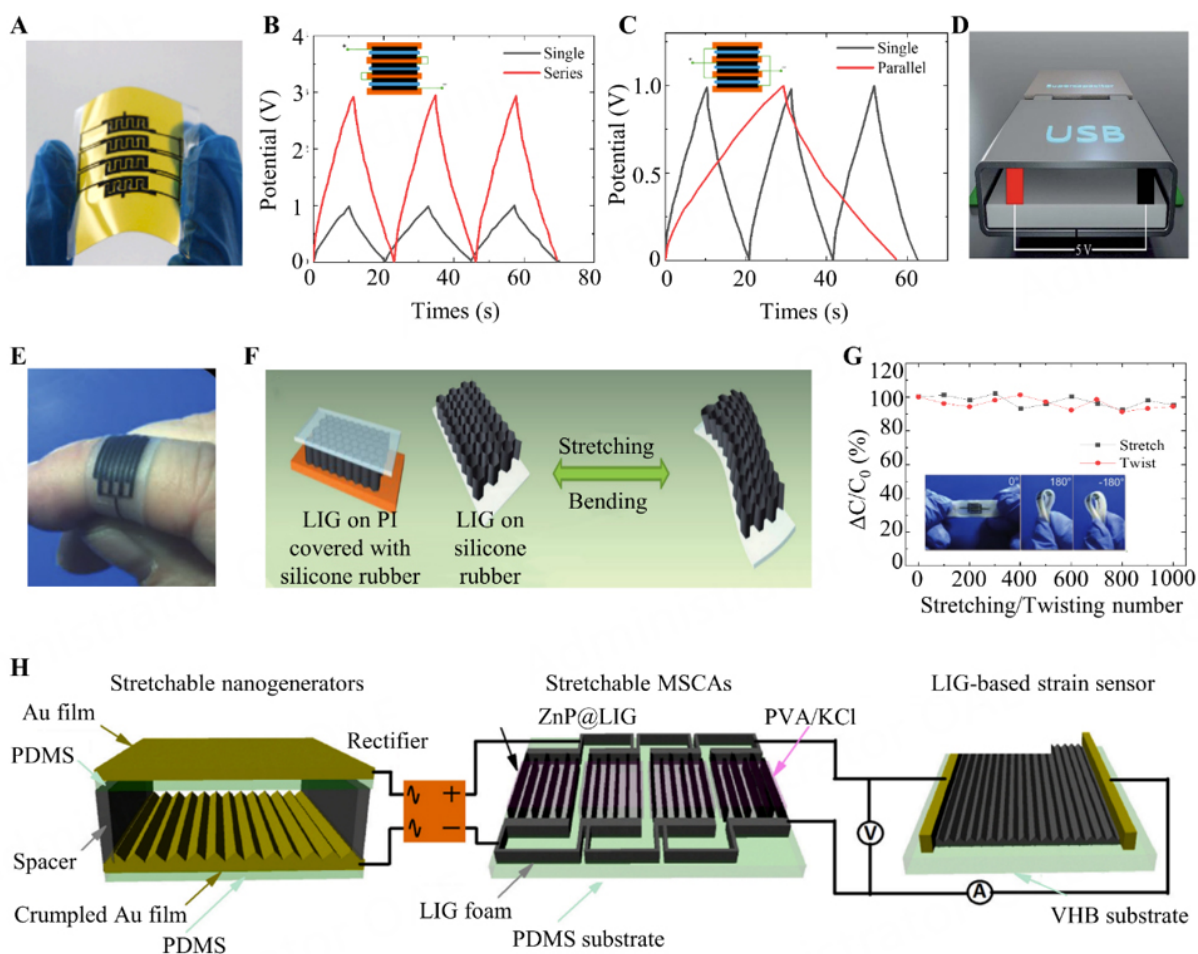


Figure 13. Design of LIG-based supercapacitor. (A) Photograph of LIG-based supercapacitor^[43]. Copyright 2021, Elsevier. (B) Comparison of cyclic charge/discharge performance of single and series-connected supercapacitors. (C) Comparison of charge/discharge performance of single and parallel-connected supercapacitors. Reproduced with permission^[169]. Copyright 2015, American Chemical Society. (D) 5 V USB charging by connecting five supercapacitors in series^[170]. Copyright 2019, American Chemical Society. (E) Photograph of LIG-based wearable supercapacitor. (F) Schematic diagram of transferring LIG to silicone rubber. (G) Cyclic test of the wearable supercapacitor (~1000 stretching and twisting cycles). Reproduced with permission^[172]. Copyright 2017, WILEY-VCH Verlag GmbH & Co. KGaA, Weinheim. (H) Schematic diagram of self-powered stretchable systems^[43]. Copyright 2021, Elsevier.

natural wood^[108]) have been proven to be used for the fabrication of the LIG electrocatalyst. Besides, the performance of the LIG electrocatalyst can be improved by heteroatom doping^[30,177,178].

Button batteries have a wide range of applications in electronic devices due to their portability. Employing the features of porous structure, hydrophilic property, and tunable electrochemical property of LIG, Aslam *et al.* prepared a button battery with LIG as the anode^[179]. Before folding, the LIG is first soaked in the electrolyte to ensure full contact of LIG electrode with the electrolyte, and then the lithium foil, electrolyte, separator, electrolyte, and LIG are stacked on the spacer to assemble the button battery, which is exhibited in Figure 14D in detail. By annealing LIG at 400 °C, the internal resistance of the button battery can be reduced [Figure 14E], enabling an improvement of reversible specific capacitances^[179]. This pioneering application opens up a new area of LIG application. Compared to traditional metal electrodes, LIG is much cheaper, which is helpful for the low-cost fabrication of the commercial button battery.

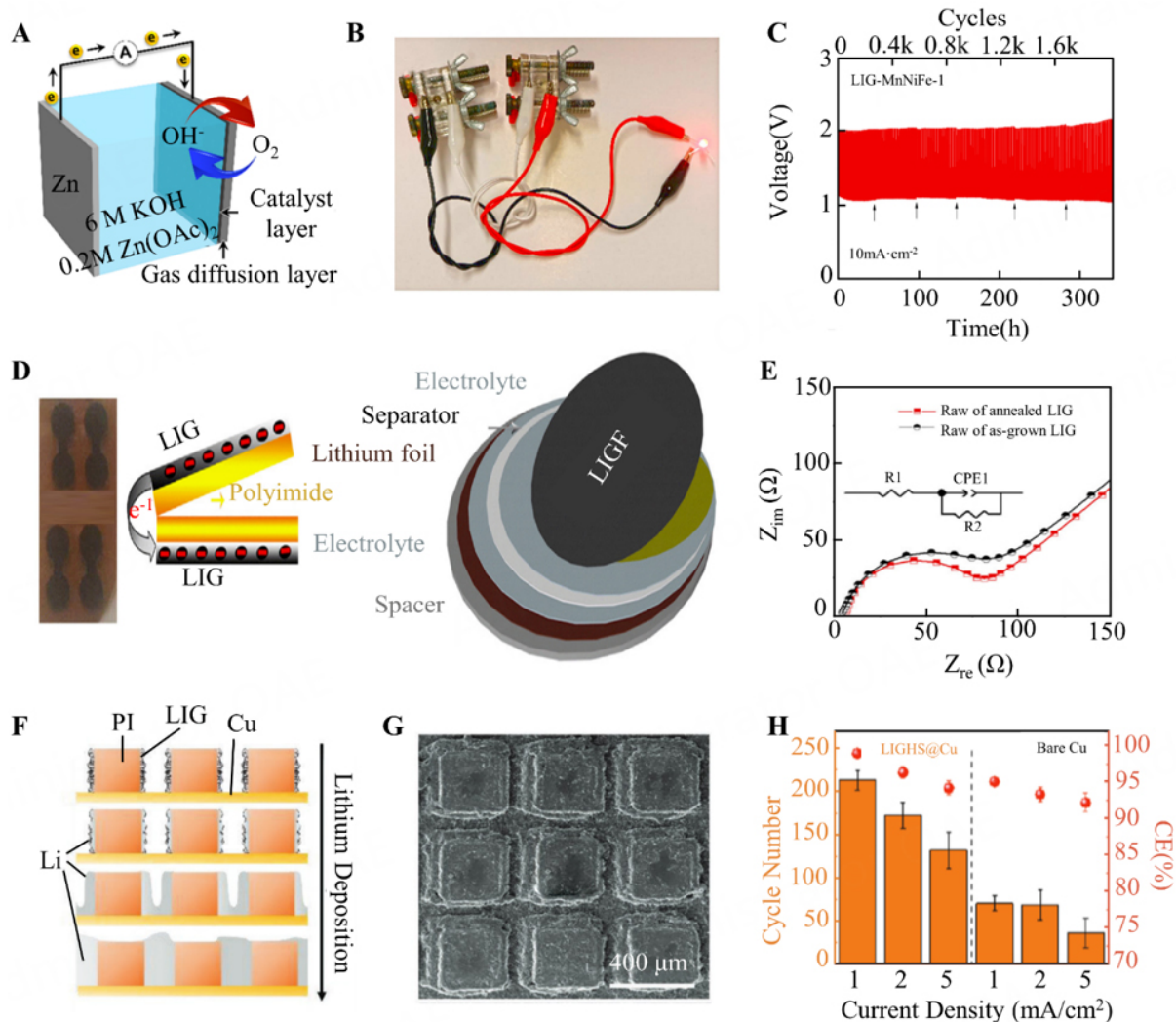


Figure 14. Application of LIG in the field of battery. (A) Schematic diagram of Zn-Air battery. (B) Two zinc-air batteries connected in series to illuminate the LED. (C) Cyclic tests of the LIG-based zinc-air battery. Reproduced with permission^[176]. Copyright 2019, American Chemical Society. (D) Schematic diagram of LIG-based button battery. (E) Effect of annealing on electrochemical impedance. Reproduced with permission^[179]. Copyright 2019, Elsevier. (F) Schematic diagram of the deposition process of Li. (G) SEM image of Li during deposition. (H) Performance comparison of deposition on LIG and bare Cu. Reproduced with permission^[180]. Copyright 2019, WILEY-VCH Verlag GmbH & Co. KGaA, Weinheim.

Although the prepared LIG has many defects, these defects are favorable to the deposition of metals, such as lithium, a common material in the battery. As a pioneering study on the use of LIG for the lithium battery, Yi *et al.* adopted LIG to regulate the nucleation and deposition of lithium, resulting in the preparation of stable lithium anodes^[180] [Figure 14F]. The lithium starts nucleation in LIG, but not on the exposed Cu surface due to the reduction of the metal nucleation overpotential and acceleration of the kinetic rate of metal nucleation [Figure 14G]. Compared to the lithium anodes grown on the bare Cu, the average Coulomb efficiency and cycle numbers of LIG-based lithium battery are much higher^[180], as shown in Figure 14H. This application demonstrates the unique advantages of LIG in the lithium battery, which can help to improve the performance of the lithium battery that is already widely used in consumer electronics.

CONCLUSION AND OUTLOOK

Laser-induced graphene, which features excellent physical and chemical properties, has attracted much attention in fundamental research and practical applications of carbon-based electronics. Particularly, due to its good flexibility, natural porous structure, fine electrical property, and excellent electrochemical property, LIG is a promising material for flexible electronics. In the past 8 years, numerous efforts have been devoted to mechanism research, preparation methods, and modification of LIG, which has pushed forward its practical applications in various flexible electronic devices.

The mechanism studies show that a high-temperature and high-pressure environment are formed on the surface of the polymer under laser irradiation. In this process, the polymer can be decomposed into graphene as long as the required situations are satisfied (temperature greater than 2700 K). The decomposition of the polymer is mainly induced by the photothermal effect for the laser with a wavelength larger than 390 nm, while for wavelengths less than this threshold, it is a coupling of photothermal and photochemical effects. Guided by the above mechanisms, the preparation of LIG has received great development, including the diversity of laser and carbon sources, and property modulation of LIG. Many experimental studies have shown that various laser sources ranging from ultraviolet laser to infrared laser, could be used for the preparation of LIG. Besides, various carbon sources (e.g., thermoset polymers, thermoplastic polymers, and natural polymers) could be selected to prepare LIG. Although the preparation process of LIG is simpler than that of the CVD method, the quality of LIG is much lower. To solve this problem, the method of property modulation has become an important and popular research direction in recent years, including process parameters, processing environment, and heteroatom doping. By altering process parameters, the hole size, LIG thickness, and square resistance can be controlled. The variation in the processing environment from oxygen-containing to oxygen-free causes a change from hydrophilic to hydrophobic, with a decrease in resistance due to the oxidation of LIG. As for the method of heteroatom doping, it is a widely used method to modulate the electrical, electrochemical, and hydrophilic/hydrophobic properties of LIG. The diversity of laser and carbon sources as well as the plentiful modification methods of LIG has contributed to the broad applications of LIG-based electronic devices [Table 2].

Facilitated by the above favorable advantages of LIG, the application of LIG-based flexible electronic devices in various fields has witnessed rapid development in recent years, which can be divided into four categories: actuators, sensors, electromagnetic devices, and energy storage devices. Due to the excellent absorption property of LIG for light, it can be used for the preparation of the photothermal actuator, thus providing a new route for the preparation of the actuator. The electrothermal actuator is also an important application for LIG flexible electronics, which can be reversibly deformed into different 3D structures, opening up new revenue for the low-cost preparation of reconfigurable soft robots. Interestingly, the defects of LIG are beneficial for sensing. For example, they help to improve the sensitivity of strain sensors, gas sensors, and pressure sensors, thus improving the performance of flexible sensors. In addition, LIG has found its applications in the field of electromagnetic devices, including radiofrequency antenna devices, electromagnetic shielding devices, terahertz wave modulators, and terahertz imaging devices. Moreover, the defects of LIG are helpful to heteroatom doping, resulting in its broad applications in the field of energy storage (e.g., supercapacitors and batteries).

Despite the favorable results mentioned above, there are four drawbacks to the preparation and application of LIG. Firstly, point-to-point exposure is time-consuming with a low processing efficiency. In particular, a multiple scanning scheme must be used for electrodes larger than the spot, thus resulting in poor homogeneity of the electrode due to the inevitable overlap of carbonization locations. Meanwhile, most LIG is prepared by laser with Gaussian spot, which results in more pronounced inhomogeneities of the

Table 2. Preparation of LIG and its application

Laser source	Carbon source	Features of LIG (thickness and square resistance)	Application	Performance	Ref.
10.6 μm laser	PDMS	200 μm	Photothermal actuator	6.6 s of continuous irradiation to drive the gear	[100]
10.6 μm laser	Ph-ddm	26 μm	Photothermal actuator	Response time of 0.48 ± 0.14 s with a velocity of 11.05 ± 0.87 mm/s	[127]
10.6 μm laser	Polyimide	35 μm	Photothermal actuator	The time required to increase the temperature from 35 $^{\circ}\text{C}$ to 75 $^{\circ}\text{C}$ is 9 s	[131]
10.6 μm laser	Polyimide	20 μm , 10 Ω/sq	Electrothermal actuator	Response time of -5 s	[130]
355 nm laser	Polyimide	5 μm	Strain sensor	Sensitivity of 19-26	[41]
10.6 μm laser	PEEK	50-60 μm	Strain sensor	Sensitivity of 212.35 (2%-5% strain)	[99]
10.6 μm laser	Polyimide	20 μm	Strain sensor	Sensitivity of 1.33 (0%-60% strain)	[134]
10.6 μm laser	Polyimide	49.2 μm	Strain sensor	Sensitivity of 12.1 (0%-5% strain)	[133]
10.6 μm laser	Polyimide	-	Gas sensor	Low detection limit of H_2 (4%)	[136]
10.6 μm laser	Phenol-formaldehyde resins	-	Gas sensor	Large response of -12%; Low detection limit of a few parts per billion	[102]
450 nm laser	Polyimide	8-60 μm	Acoustic Sensors	Broad-spectrum sound from 100 Hz-40 kHz	[145]
10.6 μm laser	Paper	-	Electromagnetic shielding device	EMI shielding efficiency of 20 dB	[155]
10.6 μm laser	Polyimide	195 μm , 327 μm	Electromagnetic shielding device	EMI shielding efficiency of 55 dB	[156]
450 nm laser	Polyimide	25.5 μm , 48.3 μm	Electromagnetic shielding device	32.7 dB	[157]
10.6 μm laser	Ph-ddm	40-70 μm	Electromagnetic shielding device	Ultrahigh shielding efficiency (SSE/t) of 240123 dB cm^2/g	[158]
450 nm laser	Polyimide	78.4 μm	Terahertz wave modulators and imaging device	Transmission of 0.8 at a frequency of 0.28 THz	[80]
10.6 μm laser	Polyimide	35 μm , 40 Ω/sq	Nanogenerator	Open-circuit voltages > 3.5 kV and peak power > 8 mW	[163]
10.6 μm laser	Polyimide	-	Nanogenerator	Voltage ramps up to 300-600 mV within 3 s	[166]
10.6 μm laser	Ecoflex	-	Nanogenerator	Maximum output power of 0.02 mW/ cm^2	[167]
10.6 μm laser	Polyimide	-	Nanogenerator	Power of 2.76 W/ m^2	[165]
405 nm laser	Polyimide	12 μm , 65 Ω/sq	Supercapacitor	21.3 F/ cm^3	[86]
405 nm laser	Phenolic resins	67 μm , 44 Ω/sq	Supercapacitor	0.78 mF/ cm^2 ; 93.78% of its initial value after 2000 cycles	[101]
450 nm laser	Polyimide	82 μm	Supercapacitor	0.62 mF/ cm^2 ; 90% of its initial value after 3000 cycles	[168]
10.6 μm laser	Polyimide	25 μm	Supercapacitor	9 mF/ cm^2 ; its initial value after 8000 cycles	[169]
1064 nm laser	Polyimide	-	Supercapacitor	998 mF/ cm^2 ; 98% of its initial value after 10,000 cycles	[170]

10.6 μm laser	Polyimide	60-70 μm	Supercapacitor	0.79 mF/cm^2 ; 96% of its initial value after 10,000 cycles	[172]
10.6 μm laser	Polyimide	100 μm	Supercapacitor	7.125 mF/cm^2	[43]
10.6 μm laser	Polyimide	-	Fuel battery	98.9 mW/cm^2 ; charge/discharge cycles for >200 h	[176]
10.6 μm laser	Polyimide	30-50 μm	Button battery	0.28 $\text{mA h}/\text{cm}^2$; coulombic efficiency of 99%	[179]
532 nm laser	Polyimide	-	Li battery	10% capacity loss over 250 cycles; coulombic efficiency of 99%	[180]

electrode. However, large-area fabrication of uniform electrodes is important in certain applications, such as conducting polymer films for the electrochemical removal of heavy metal contaminants^[181]. Secondly, although some methods (e.g., layer-by-layer ablation^[182] and laminated object manufacturing^[183]) have been developed to fabricate various 3D structures of LIG, LIG-based integrated circuits with 3D structures have rarely been reported. One important reason is the poor electrical property of pure LIG. Currently, composite electrodes of LIG/metal exhibit electrical property close to those of metals, but at the expense of fabrication time and cost. In the future, more efforts should be devoted to the study of the carbonization mechanism, thus enabling high-conductive LIG without metal doping. Thirdly, the main problem with commercializing self-powered LIG-based systems is that they cannot work for long periods of time. Therefore, high-efficient LIG-based nanogenerators and low-energy-consumption electronic devices are necessary for its large-scale industrial application in the future. Finally, for wearable/implantable electronic devices, the toxicity of LIG to humans is not known, which should be carefully investigated in the future. With the continuous endeavors in this field, LIG-based flexible electronic devices will have brighter application prospects.

DECLARATIONS

Authors' contributions

Did the literature review, outlined the manuscript structure, and wrote the manuscript draft: Yu H, Gai M

Participated in the discussion of the review content: Liu L, Chen F, Bian J, Huang Y

Initiated the reviewing idea and were involved in the discussion and revision of the manuscript: Yu H, Bian J

All authors have read the manuscript and approved the final version.

Availability of data and materials

Not applicable.

Financial support and sponsorship

This study was supported by the National Key Research and Development Program Grant of China (2020YFA0405700), the National Natural Science Foundation of China (51925503, 52105576, 52188102), and the Natural Science Foundation of Hubei Province of China (2020CFA028).

Conflicts of interest

All authors declared that there are no conflicts of interest.

Ethical approval and consent to participate

Not applicable.

Consent for publication

Not applicable.

Copyright

© The Author(s) 2023.

REFERENCES

1. Pisana S, Lazzeri M, Casiraghi C, et al. Breakdown of the adiabatic Born-Oppenheimer approximation in graphene. *Nat Mater* 2007;6:198-201. [DOI](#) [PubMed](#)
2. Geim AK, Novoselov KS. The rise of graphene. *Nat Mater* 2007;6:183-91. [DOI](#) [PubMed](#)
3. Nair RR, Blake P, Grigorenko AN, et al. Fine structure constant defines visual transparency of graphene. *Science* 2008;320:1308. [DOI](#) [PubMed](#)
4. Lee C, Wei X, Kysar JW, Hone J. Measurement of the elastic properties and intrinsic strength of monolayer graphene. *Science* 2008;321:385-8. [DOI](#) [PubMed](#)
5. Liu T, Asheghi M, Goodson KE. Performance and manufacturing of silicon-based vapor chambers. *Appl Mech Rev* 2021;73:010802. [DOI](#)
6. Zhu Y, Schenk M, Filipov ET. A review on origami simulations: from kinematics, to mechanics, toward multiphysics. *Appl Mech Rev* 2022;74:030801. [DOI](#)
7. Carcavilla A, Zaki W. Fatigue of shape memory alloys with emphasis on additively manufactured NiTi components. *Appl Mech Rev* 2022;74:040801. [DOI](#)
8. Novoselov KS, Geim AK, Morozov SV, et al. Electric field effect in atomically thin carbon films. *Science* 2004;306:666-9. [DOI](#) [PubMed](#)
9. Yi M, Shen Z. A review on mechanical exfoliation for the scalable production of graphene. *J Mater Chem A* 2015;3:11700-15. [DOI](#)
10. Huang Y, Pan YH, Yang R, et al. Universal mechanical exfoliation of large-area 2D crystals. *Nat Commun* 2020;11:2453. [DOI](#)
11. Chang YM, Kim H, Lee JH, et al. Multilayered graphene efficiently formed by mechanical exfoliation for nonlinear saturable absorbers in fiber mode-locked lasers. *Appl Phys Lett* 2010;97:211102. [DOI](#)
12. Soldano C, Mahmood A, Dujardin E. Production, properties and potential of graphene. *Carbon* 2010;48:2127-50. [DOI](#)
13. Zhang Y, Zhang L, Zhou C. Review of chemical vapor deposition of graphene and related applications. *ACC Chem Res* 2013;46:2329-39. [DOI](#) [PubMed](#)
14. Sun J, Chen Y, Priyadarshi MK, et al. Direct chemical vapor deposition-derived graphene glasses targeting wide ranged applications. *Nano Lett* 2015;15:5846-54. [DOI](#) [PubMed](#)
15. Sun J, Chen Z, Yuan L, et al. Direct chemical-vapor-deposition-fabricated, large-scale graphene glass with high carrier mobility and uniformity for touch panel applications. *ACS Nano* 2016;10:11136-44. [DOI](#) [PubMed](#)
16. Cui L, Chen X, Liu B, et al. Highly conductive nitrogen-doped graphene grown on glass toward electrochromic applications. *ACS Appl Mater Interfaces* 2018;10:32622-30. [DOI](#) [PubMed](#)
17. Yang W, Chen G, Shi Z, et al. Epitaxial growth of single-domain graphene on hexagonal boron nitride. *Nat Mater* 2013;12:792-7. [DOI](#) [PubMed](#)
18. Gao M, Pan Y, Huang L, et al. Epitaxial growth and structural property of graphene on Pt(111). *Appl Phys Lett* 2011;98:033101. [DOI](#)
19. Xu X, Zhang Z, Dong J, et al. Ultrafast epitaxial growth of metre-sized single-crystal graphene on industrial Cu foil. *Sci Bull* 2017;62:1074-80. [DOI](#)
20. Lee S, Toney MF, Ko W, et al. Laser-synthesized epitaxial graphene. *ACS Nano* 2010;4:7524-30. [DOI](#) [PubMed](#)
21. Pei S, Cheng H. The reduction of graphene oxide. *Carbon* 2012;50:3210-28. [DOI](#)
22. Dimiev AM, Tour JM. Mechanism of graphene oxide formation. *ACS Nano* 2014;8:3060-8. [DOI](#) [PubMed](#)
23. Hernandez Y, Nicolosi V, Lotya M, et al. High-yield production of graphene by liquid-phase exfoliation of graphite. *Nat Nanotechnol* 2008;3:563-8. [DOI](#) [PubMed](#)
24. Deng B, Liu Z, Peng H. Toward mass production of CVD graphene films. *Adv Mater* 2019;31:e1800996. [DOI](#) [PubMed](#)
25. Paredes JI, Villar-Rodil S, Martínez-Alonso A, Tascón JM. Graphene oxide dispersions in organic solvents. *Langmuir* 2008;24:10560-4. [DOI](#) [PubMed](#)
26. Han DD, Zhang YL, Ma JN, Liu YQ, Han B, Sun HB. Light-mediated manufacture and manipulation of actuators. *Adv Mater*

- 2016;28:8328-43. [DOI](#) [PubMed](#)
27. Hummers WS Jr, Offeman RE. Preparation of graphitic oxide. *J Am Chem Soc* 1958;80:1339. [DOI](#)
28. Yu W, Sisi L, Haiyan Y, Jie L. Progress in the functional modification of graphene/graphene oxide: a review. *RSC Adv* 2020;10:15328-45. [DOI](#) [PubMed](#) [PMC](#)
29. Lin J, Peng Z, Liu Y, et al. Laser-induced porous graphene films from commercial polymers. *Nat Commun* 2014;5:5714. [DOI](#) [PubMed](#) [PMC](#)
30. Singh SP, Li Y, Zhang J, Tour JM, Arnusch CJ. Sulfur-doped laser-induced porous graphene derived from polysulfone-class polymers and membranes. *ACS Nano* 2018;12:289-97. [DOI](#) [PubMed](#)
31. Wan Z, Umer M, Lobino M, et al. Laser induced self-N-doped porous graphene as an electrochemical biosensor for femtomolar miRNA detection. *Carbon* 2020;163:385-94. [DOI](#)
32. Ye R, James DK, Tour JM. Laser-induced graphene. *ACC Chem Res* 2018;51:1609-20. [DOI](#) [PubMed](#)
33. Huang L, Su J, Song Y, Ye R. Laser-induced graphene: en route to smart sensing. *Nano-Micro Lett* 2020;12:157. [DOI](#) [PubMed](#) [PMC](#)
34. Ye X, Long J, Lin Z, Zhang H, Zhu H, Zhong M. Direct laser fabrication of large-area and patterned graphene at room temperature. *Carbon* 2014;68:784-90. [DOI](#)
35. Lamberti A, Clerici F, Fontana M, Scaltrito L. A highly stretchable supercapacitor using laser-induced graphene electrodes onto elastomeric substrate. *Adv Energy Mater* 2016;6:1600050. [DOI](#)
36. Sha Y, Yang W, Li S, et al. Laser induced graphitization of PAN-based carbon fibers. *RSC Adv* 2018;8:11543-50. [DOI](#) [PubMed](#) [PMC](#)
37. Lamberti A, Perrucci F, Caprioli M, et al. New insights on laser-induced graphene electrodes for flexible supercapacitors: tunable morphology and physical properties. *Nanotechnology* 2017;28:174002. [DOI](#) [PubMed](#)
38. Liu J, Liu H, Lin N, et al. Facile fabrication of super-hydrophilic porous graphene with ultra-fast spreading feature and capillary effect by direct laser writing. *Mater Chem Phys* 2020;251:123083. [DOI](#)
39. Nasser J, Groo L, Zhang L, Sodano H. Laser induced graphene fibers for multifunctional aramid fiber reinforced composite. *Carbon* 2020;158:146-56. [DOI](#)
40. Jeong SY, Ma YW, Lee JU, Je GJ, Shin BS. Flexible and highly sensitive strain sensor based on laser-induced graphene pattern fabricated by 355 nm pulsed laser. *Sensors* 2019;19:4867. [DOI](#) [PubMed](#) [PMC](#)
41. Carvalho AF, Fernandes AJS, Leitão C, et al. Laser-induced graphene strain sensors produced by ultraviolet irradiation of polyimide. *Adv Funct Mater* 2018;28:1805271. [DOI](#)
42. Stanford MG, Zhang C, Fowlkes JD, et al. High-resolution laser-induced graphene. flexible electronics beyond the visible limit. *ACS Appl Mater Interfaces* 2020;12:10902-7. [DOI](#)
43. Zhang C, Peng Z, Huang C, et al. High-energy all-in-one stretchable micro-supercapacitor arrays based on 3D laser-induced graphene foams decorated with mesoporous ZnP nanosheets for self-powered stretchable systems. *Nano Energy* 2021;81:105609. [DOI](#)
44. Abdulhafez M, Tomaraei GN, Bedewy M. Fluence-dependent morphological transitions in laser-induced graphene electrodes on polyimide substrates for flexible devices. *ACS Appl Nano Mater* 2021;4:2973-86. [DOI](#)
45. Huang Y, Zeng L, Liu C, et al. Laser direct writing of heteroatom (N and S)-doped graphene from a polybenzimidazole ink donor on polyethylene terephthalate polymer and glass substrates. *Small* 2018;14:e1803143. [DOI](#) [PubMed](#)
46. Wang H, Zhao Z, Liu P, Guo X. A soft and stretchable electronics using laser-induced graphene on polyimide/PDMS composite substrate. *NPJ Flex Electron* 2022;6. [DOI](#)
47. Huang L, Wang H, Zhan D, Fang F. Flexible capacitive pressure sensor based on laser-induced graphene and polydimethylsiloxane foam. *IEEE Sensors J* 2021;21:12048-56. [DOI](#)
48. Joanni E, Kumar R, Fernandes WP, Savu R, Matsuda A. In situ growth of laser-induced graphene micro-patterns on arbitrary substrates. *Nanoscale* 2022;14:8914-8. [DOI](#) [PubMed](#)
49. Kulyk B, Silva BFR, Carvalho AF, et al. Laser-induced graphene from paper by ultraviolet irradiation: humidity and temperature sensors. *Adv Mater Technol* 2022;7:2101311. [DOI](#)
50. He M, Wang G, Zhu Y, Wang Y, Liu F, Luo S. In-situ joule heating-triggered nanopores generation in laser-induced graphene papers for capacitive enhancement. *Carbon* 2022;186:215-26. [DOI](#)
51. Wang D, Li J, Wang Y, et al. Laser-induced graphene papers with tunable microstructures as antibacterial agents. *ACS Appl Nano Mater* 2022. [DOI](#)
52. Ye R, James DK, Tour JM. Laser-induced graphene: from discovery to translation. *Adv Mater* 2019;31:e1803621. [DOI](#) [PubMed](#)
53. Wang H, Zhao Z, Liu P, Guo X. Laser-Induced graphene based flexible electronic devices. *Biosensors* 2022;12:55. [DOI](#) [PubMed](#) [PMC](#)
54. You R, Liu YQ, Hao YL, et al. Laser fabrication of graphene-based flexible electronics. *Adv Mater* 2020;32:1901981. [DOI](#)
55. Smirnov VA, Arbuzov AA, Shul'ga YM, et al. Photoreduction of graphite oxide. *High Energy Chem* 2011;45:57-61. [DOI](#)
56. Moon HK, Lee SH, Choi HC. In vivo near-infrared mediated tumor destruction by photothermal effect of carbon nanotubes. *ACS Nano* 2009;3:3707-13. [DOI](#) [PubMed](#)
57. Qian D, Wagner GJ, Liu WK, Yu M, Ruoff RS. Mechanics of carbon nanotubes. *Appl Mech Rev* 2002;55:495-533. [DOI](#)
58. Ehsani H, Boyd JD, Wang J, Grady ME. Evolution of the laser-induced spallation technique in film adhesion measurement. *Appl Mech Rev* 2021;73:030802. [DOI](#) [PubMed](#) [PMC](#)

59. Mukherjee R, Thomas AV, Krishnamurthy A, Koratkar N. Photothermally reduced graphene as high-power anodes for lithium-ion batteries. *ACS Nano* 2012;6:7867-78. DOI PubMed
60. Li G. Direct laser writing of graphene electrodes. *J Appl Phys* 2020;127:010901. DOI
61. Treyz GV, Scarmozzino R, Osgood RM. Deep ultraviolet laser etching of vias in polyimide films. *Appl Phys Lett* 1989;55:346-8. DOI
62. Ruan X, Wang R, Luo J, Yao Y, Liu T. Experimental and modeling study of CO₂ laser writing induced polyimide carbonization process. *Mater Des* 2018;160:1168-77. DOI
63. Bian J, Chen F, Ling H, et al. Experimental and modeling study of controllable laser lift-off via low-fluence multiscanning of polyimide-substrate interface. *Int J Heat Mass Transfer* 2022;188:122609. DOI
64. Li G, Mo X, Law WC, Chan KC. Wearable fluid capture devices for electrochemical sensing of sweat. *ACS Appl Mater Interfaces* 2019;11:238-43. DOI PubMed
65. Kim Y, Noh Y, Park S, Kim B, June Kim H. Ablation of polyimide thin-film on carrier glass using 355 nm and 37 ns laser pulses. *Int J Heat Mass Transfer* 2020;147:118896. DOI
66. Babu SV, D'coutho GC, Egitto FD. Excimer laser induced ablation of polyetheretherketone, polyimide, and polytetrafluoroethylene. *J Appl Phys* 1992;72:692-8. DOI
67. Feng Y, Liu Z, Yi X. Co-occurrence of photochemical and thermal effects during laser polymer ablation via a 248-nm excimer laser. *Appl Surf Sci* 2000;156:177-82. DOI
68. Smith GP, Crosley DR. A photochemical model of ozone interference effects in laser detection of tropospheric OH. *J Geophys Res* 1990;95:16427. DOI
69. Sutcliffe E, Srinivasan R. Dynamics of UV laser ablation of organic polymer surfaces. *J Appl Phys* 1986;60:3315-22. DOI
70. Dyer PE, Sidhu J. Excimer laser ablation and thermal coupling efficiency to polymer films. *J Appl Phys* 1985;57:1420-2. DOI
71. Gorodetsky G, Kazayaka TG, Melcher RL, Srinivasan R. Calorimetric and acoustic study of ultraviolet laser ablation of polymers. *Appl Phys Lett* 1985;46:828-30. DOI
72. Dong Y, Rismiller SC, Lin J. Molecular dynamic simulation of layered graphene clusters formation from polyimides under extreme conditions. *Carbon* 2016;104:47-55. DOI
73. Vashisth A, Kowalik M, Gerringer JC, Ashraf C, van Duin ACT, Green MJ. ReaxFF simulations of laser-induced graphene (LIG) formation for multifunctional polymer nanocomposites. *ACS Appl Nano Mater* 2020;3:1881-90. DOI
74. Singleton DL, Paraskevopoulos G, Irwin RS. XeCl laser ablation of polyimide: Influence of ambient atmosphere on particulate and gaseous products. *J Appl Phys* 1989;66:3324-8. DOI
75. Srinivasan R, Hall R, Wilson W, Loehle W, Allbee D. Ultraviolet laser irradiation of the polyimide, PMDA-ODA (Kapton™), to yield a patternable, porous, electrically conducting carbon network. *Synth Met* 1994;66:301-7. DOI
76. Raimondi F, Abolhassani S, Brüttsch R, et al. Quantification of polyimide carbonization after laser ablation. *J Appl Phys* 2000;88:3659-66. DOI
77. Srinivasan R, Hall RR, Loehle WD, Wilson WD, Allbee DC. Chemical transformations of the polyimide Kapton brought about by ultraviolet laser radiation. *J Appl Phys* 1995;78:4881-7. DOI
78. Qin Z, He T, Zhang Y. Characteristics of the conductive polyimide film surfaces induced by ultraviolet laser beam. *Appl Phys A* 1998;66:441-3. DOI
79. Duy LX, Peng Z, Li Y, Zhang J, Ji Y, Tour JM. Laser-induced graphene fibers. *Carbon* 2018;126:472-9. DOI
80. Wang Z, Wang G, Liu W, Hu B, Liu J, Zhang Y. Patterned laser-induced graphene for terahertz wave modulation. *J Opt Soc Am B* 2020;37:546. DOI
81. Lu Z, Wu L, Dai X, et al. Novel flexible bifunctional amperometric biosensor based on laser engraved porous graphene array electrodes: highly sensitive electrochemical determination of hydrogen peroxide and glucose. *J Hazard Mater* 2021;402:123774. DOI PubMed
82. Wang Z, Chen B, Sun S, Pan L, Gao Y. Maskless formation of conductive carbon layer on leather for highly sensitive flexible strain sensors. *Adv Electron Mater* 2020;6:2000549. DOI
83. Chen Y, Long J, Zhou S, et al. UV Laser-induced polyimide-to-graphene conversion: modeling, fabrication, and application. *Small Methods* 2019;3:1900208. DOI
84. Wang L, Wang Z, Bakhtiyari AN, Zheng H. A comparative study of laser-induced graphene by CO₂ infrared laser and 355 nm ultraviolet (UV) laser. *Micromachines* 2020;11:1094. DOI
85. Luo S, Hoang PT, Liu T. Direct laser writing for creating porous graphitic structures and their use for flexible and highly sensitive sensor and sensor arrays. *Carbon* 2016;96:522-31. DOI
86. Cai J, Lv C, Watanabe A. Laser direct writing of high-performance flexible all-solid-state carbon micro-supercapacitors for an on-chip self-powered photodetection system. *Nano Energy* 2016;30:790-800. DOI
87. Li G, Law W, Chan KC. Floating, highly efficient, and scalable graphene membranes for seawater desalination using solar energy. *Green Chem* 2018;20:3689-95. DOI
88. Lu X, Wu G, Xiong Q, et al. Laser in-situ synthesis of SnO₂/N-doped graphene nanocomposite with enhanced lithium storage properties based on both alloying and insertion reactions. *Appl Surf Sci* 2017;422:645-53. DOI
89. Gao Y, Li Q, Wu R, Sha J, Lu Y, Xuan F. Laser direct writing of ultrahigh sensitive SiC-based strain sensor arrays on elastomer toward electronic skins. *Adv Funct Mater* 2019;29:1806786. DOI

90. Settu K, Chiu PT, Huang YM. Laser-induced graphene-based enzymatic biosensor for glucose detection. *Polymers* 2021;13:2795. DOI PubMed PMC
91. Zhang C, Ping J, Ying Y. Evaluation of trans-resveratrol level in grape wine using laser-induced porous graphene-based electrochemical sensor. *Sci Total Environ* 2020;714:136687. DOI PubMed
92. Vanegas DC, Patiño L, Mendez C, et al. Laser scribed graphene biosensor for detection of biogenic amines in food samples using locally sourced materials. *Biosensors* 2018;8:42. DOI PubMed PMC
93. Garland NT, McLamore ES, Cavallaro ND, et al. Flexible laser-induced graphene for nitrogen sensing in soil. *ACS Appl Mater Interfaces* 2018;10:39124-33. DOI PubMed
94. Le TD, Park S, An J, Lee PS, Kim Y. Ultrafast laser pulses enable one-step graphene patterning on woods and leaves for green electronics. *Adv Funct Mater* 2019;29:1902771. DOI
95. Kalita G, Qi L, Namba Y, Wakita K, Umeno M. Femtosecond laser induced micropatterning of graphene film. *Mater Lett* 2011;65:1569-72. DOI
96. Yu H, Bian J, Chen F, Ji J, Huang Y. Ultrathin, graphene-in-polyimide strain sensor via laser-induced interfacial ablation of polyimide. *Adv Electron Mater* 2022:2201086. DOI
97. Lippert T, Ortelli E, Panitz JC, et al. Imaging-XPS/Raman investigation on the carbonization of polyimide after irradiation at 308 nm. *Appl Phys A* 1999;69:S651-S654. DOI
98. Le TH, Yang Y, Yu L, Gao T, Huang Z, Kang F. Polyimide-based porous hollow carbon nanofibers for supercapacitor electrode. *J Appl Polym Sci* 2016:133. DOI
99. Yang W, Zhao W, Li Q, et al. Fabrication of smart components by 3D printing and laser-scribing technologies. *ACS Appl Mater Interfaces* 2020;12:3928-35. DOI PubMed
100. Wang W, Liu Y, Liu Y, et al. Direct laser writing of superhydrophobic PDMS elastomers for controllable manipulation via marangoni effect. *Adv Funct Mater* 2017;27:1702946. DOI
101. Zhang Z, Song M, Hao J, Wu K, Li C, Hu C. Visible light laser-induced graphene from phenolic resin: a new approach for directly writing graphene-based electrochemical devices on various substrates. *Carbon* 2018;127:287-96. DOI
102. Yang L, Ji H, Meng C, et al. Intrinsically breathable and flexible NO₂ gas sensors produced by laser direct writing of self-assembled block copolymers. *ACS Appl Mater Interfaces* 2022;14:17818-25. DOI PubMed
103. Yang L, Yan J, Meng C, et al. Vanadium oxide-doped laser-induced graphene multi-parameter sensor to decouple soil nitrogen loss and temperature. *Res Square* 2022;2210322. DOI
104. Beckham JL, Li JT, Stanford MG, et al. High-resolution laser-induced graphene from photoresist. *ACS Nano* 2021;15:8976-83. DOI PubMed
105. Ye R, Han X, Kosynkin DV, et al. Laser-induced conversion of teflon into fluorinated nanodiamonds or fluorinated graphene. *ACS Nano* 2018;12:1083-8. DOI
106. Sharma CP, Arnusch CJ. Laser-induced graphene composite adhesive tape with electro-photo-thermal heating and antimicrobial capabilities. *Carbon* 2022;196:102-9. DOI
107. Long CT, Oh JH, Martinez AD, et al. Polymer infiltration and pyrolysis cycling for creating dense, conductive laser-induced graphene. *Carbon* 2022;200:264-70. DOI
108. Ye R, Chyan Y, Zhang J, et al. Laser-induced graphene formation on wood. *Adv Mater* 2017;29:1702211. DOI PubMed
109. Dreimol CH, Guo H, Ritter M, et al. Sustainable wood electronics by iron-catalyzed laser-induced graphitization for large-scale applications. *Nat Commun* 2022;13:3680. DOI PubMed PMC
110. Chyan Y, Ye R, Li Y, Singh SP, Arnusch CJ, Tour JM. Laser-induced graphene by multiple lasing: toward electronics on cloth, paper, and food. *ACS Nano* 2018;12:2176-83. DOI PubMed
111. Wang S, Yu Y, Luo S, et al. All-solid-state supercapacitors from natural lignin-based composite film by laser direct writing. *Appl Phys Lett* 2019;115:083904. DOI
112. Liu M, Wu J, Cheng H. Effects of laser processing parameters on properties of laser-induced graphene by irradiating CO₂ laser on polyimide. *Sci China Technol Sci* 2022;65:41-52. DOI
113. Li Y, Luong DX, Zhang J, et al. Laser-induced graphene in controlled atmospheres: from superhydrophilic to superhydrophobic surfaces. *Adv Mater* 2017;29:1700496. DOI PubMed
114. Xu B, Ding Y. Hydrophilic/Hydrophobic SiO₂ nanoparticles enabled janus-type paper through commercial glaco spraying and air-plasma treatment. *Adv Mater Interfaces* 2022;9:2200934. DOI
115. Bodas D, Khan-malek C. Formation of more stable hydrophilic surfaces of PDMS by plasma and chemical treatments. *Microelectron Eng* 2006;83:1277-9. DOI
116. Chen Y, Xie B, Long J, et al. Interfacial laser-induced graphene enabling high-performance liquid-solid triboelectric nanogenerator. *Adv Mater* 2021;33:e2104290. DOI PubMed
117. Han X, Ye R, Chyan Y, et al. Laser-induced graphene from wood impregnated with metal salts and use in electrocatalysis. *ACS Appl Nano Mater* 2018;1:5053-61. DOI
118. Deng H, Zhang C, Xie Y, et al. Laser induced MoS₂/carbon hybrids for hydrogen evolution reaction catalysts. *J Mater Chem A* 2016;4:6824-30. DOI
119. Peng Z, Jia J, Ding H, et al. High-energy all-in-one micro-supercapacitors based on ZnO mesoporous nanosheet-decorated laser-induced porous graphene foams. *J Mater Res* 2021;36:1927-36. DOI

120. Yi T, Mei J, Guan B, et al. Construction of spherical NiO@MnO₂ with core-shell structure obtained by depositing MnO₂ nanoparticles on NiO nanosheets for high-performance supercapacitor. *Ceram Int* 2020;46:421-9. [DOI](#)
121. Amiri MH, Namdar N, Mashayekhi A, Ghasemi F, Sanaee Z, Mohajerzadeh S. Flexible micro supercapacitors based on laser-scribed graphene/ZnO nanocomposite. *J Nanopart Res* 2016;18. [DOI](#)
122. Zhu J, Liu S, Hu Z, et al. Laser-induced graphene non-enzymatic glucose sensors for on-body measurements. *Biosens Bioelectron* 2021;193:113606. [DOI](#) [PubMed](#) [PMC](#)
123. Rahimi R, Ochoa M, Ziaie B. Direct Laser Writing of porous-carbon/silver nanocomposite for flexible electronics. *ACS Appl Mater Interfaces* 2016;8:16907-13. [DOI](#) [PubMed](#)
124. Hermerschmidt F, Burmeister D, Ligorio G, et al. Truly low temperature sintering of printed copper ink using formic acid. *Adv Mater Technol* 2018;3:1800146. [DOI](#)
125. Chang H, Guo R, Sun Z, et al. Direct writing and repairable paper flexible electronics using nickel-liquid metal ink. *Adv Mater Interfaces* 2018;5:1800571. [DOI](#)
126. Eshkalak S, Chinnappan A, Jayathilaka W, Khatibzadeh M, Kowsari E, Ramakrishna S. A review on inkjet printing of CNT composites for smart applications. *Appl Mater Today* 2017;9:372-86. [DOI](#)
127. Peng Y, Zhao W, Ni F, Yu W, Liu X. Forest-like laser-induced graphene film with ultrahigh solar energy utilization efficiency. *ACS Nano* 2021;15:19490-502. [DOI](#) [PubMed](#)
128. Zhao P, Bhattacharya G, Fishlock SJ, et al. Replacing the metal electrodes in triboelectric nanogenerators: high-performance laser-induced graphene electrodes. *Nano Energy* 2020;75:104958. [DOI](#)
129. Xu Y, Fei Q, Page M, et al. Laser-induced graphene for bioelectronics and soft actuators. *Nano Res* 2021;14:3033-50. [DOI](#) [PubMed](#) [PMC](#)
130. Ling Y, Pang W, Li X, et al. Laser-induced graphene for electrothermally controlled, mechanically guided, 3D assembly and human-soft actuators interaction. *Adv Mater* 2020;32:e1908475. [DOI](#) [PubMed](#)
131. Wang W, Han B, Zhang Y, et al. Laser-induced graphene tapes as origami and stick-on labels for photothermal manipulation via marangoni effect. *Adv Funct Mater* 2021;31:2006179. [DOI](#)
132. Rahimi R, Ochoa M, Yu W, Ziaie B. Highly stretchable and sensitive unidirectional strain sensor via laser carbonization. *ACS Appl Mater Interfaces* 2015;7:4463-70. [DOI](#) [PubMed](#)
133. Chen X, Luo F, Yuan M, et al. A dual-functional graphene-based self-alarm health-monitoring e-skin. *Adv Funct Mater* 2019;29:1904706. [DOI](#)
134. Sun B, McCay RN, Goswami S, et al. Gas-permeable, multifunctional on-skin electronics based on laser-induced porous graphene and sugar-templated elastomer sponges. *Adv Mater* 2018;30:e1804327. [DOI](#) [PubMed](#)
135. Chen X, Li R, Niu G, et al. Porous graphene foam composite-based dual-mode sensors for underwater temperature and subtle motion detection. *Chem Eng J* 2022;444:136631. [DOI](#)
136. Zhu J, Cho M, Li Y, et al. Biomimetic turbinate-like artificial nose for hydrogen detection based on 3D porous laser-induced graphene. *ACS Appl Mater Interfaces* 2019;11:24386-94. [DOI](#) [PubMed](#)
137. Cheng L, Guo W, Cao X, et al. Laser-induced graphene for environmental applications: progress and opportunities. *Mater Chem Front* 2021;5:4874-91. [DOI](#)
138. Yang L, Yi N, Zhu J, et al. Novel gas sensing platform based on a stretchable laser-induced graphene pattern with self-heating capabilities. *J Mater Chem A* 2020;8:6487-500. [DOI](#)
139. Stanford MG, Yang K, Chyan Y, Kittrell C, Tour JM. Laser-Induced graphene for flexible and embeddable gas sensors. *ACS Nano* 2019;13:3474-82. [DOI](#) [PubMed](#)
140. Dosi M, Lau I, Zhuang Y, Simakov DSA, Fowler MW, Pope MA. Ultrasensitive electrochemical methane sensors based on solid polymer electrolyte-infused laser-induced graphene. *ACS Appl Mater Interfaces* 2019;11:6166-73. [DOI](#) [PubMed](#)
141. Kaidarova A, Alsharif N, Oliveira BNM, et al. Laser-printed, flexible graphene pressure sensors. *Global Challenges* 2020;4:2000001. [DOI](#) [PubMed](#) [PMC](#)
142. Zhu C, Guo D, Ye D, Jiang S, Huang Y. Flexible PZT-integrated, bilateral sensors via transfer-free laser lift-off for multimodal measurements. *ACS Appl Mater Interfaces* 2020;12:37354-62. [DOI](#) [PubMed](#)
143. Ju K, Gao Y, Xiao T, Yu C, Tan J, Xuan F. Laser direct writing of carbonaceous sensors on cardboard for human health and indoor environment monitoring. *RSC Adv* 2020;10:18694-703. [DOI](#) [PubMed](#) [PMC](#)
144. Yang L, Wang H, Yuan W, et al. Wearable pressure sensors based on MXene/tissue papers for wireless human health monitoring. *ACS Appl Mater Interfaces* 2021;13:60531-43. [DOI](#) [PubMed](#)
145. Wang X, Gu Y, Xiong Z, Cui Z, Zhang T. Silk-molded flexible, ultrasensitive, and highly stable electronic skin for monitoring human physiological signals. *Adv Mater* 2014;26:1336-42. [DOI](#) [PubMed](#)
146. Gong S, Schwab W, Wang Y, et al. A wearable and highly sensitive pressure sensor with ultrathin gold nanowires. *Nat Commun* 2014;5:1-8. [DOI](#) [PubMed](#)
147. Wang Q, Jian M, Wang C, Zhang Y. Carbonized silk nanofiber membrane for transparent and sensitive electronic skin. *Adv Funct Mater* 2017;27:1605657. [DOI](#)
148. Chun S, Jung H, Choi Y, Bae G, Kil JP, Park W. A tactile sensor using a graphene film formed by the reduced graphene oxide flakes and its detection of surface morphology. *Carbon* 2015;94:982-7. [DOI](#)
149. Duan S, Wang B, Lin Y, et al. Waterproof mechanically robust multifunctional conformal sensors for underwater interactive human-

- machine interfaces. *Adv Intell Syst* 2021;3:2100056. DOI
150. Tao LQ, Tian H, Liu Y, et al. An intelligent artificial throat with sound-sensing ability based on laser induced graphene. *Nat Commun* 2017;8:14579. DOI PubMed PMC
151. Zhang S, Zhu J, Zhang Y, et al. Standalone stretchable RF systems based on asymmetric 3D microstrip antennas with on-body wireless communication and energy harvesting. *Nano Energy* 2022;96:107069. DOI
152. Zhu J, Zhang S, Yi N, et al. Strain-insensitive hierarchically structured stretchable microstrip antennas for robust wireless communication. *Nanomicro Lett* 2021;13:108. DOI PubMed PMC
153. Zhu J, Hu Z, Song C, et al. Stretchable wideband dipole antennas and rectennas for RF energy harvesting. *Mater Today Phys* 2021;18:100377. DOI PubMed PMC
154. Zhu J, Hu Z, Zhang S, et al. Stretchable 3D wideband dipole antennas from mechanical assembly for on-body communication. *ACS Appl Mater Interfaces* 2022;14:12855-62. DOI PubMed
155. Zang X, Xing D, Tang W, et al. Electromagnetic interference shielding with laser induced molybdenum carbide-graphene paper. *Mater Lett* 2020;271:127784. DOI
156. Yin J, Zhang J, Zhang S, et al. Flexible 3D porous graphene film decorated with nickel nanoparticles for absorption-dominated electromagnetic interference shielding. *Chem Eng J* 2021;421:129763. DOI
157. Xu J, Li R, Ji S, et al. Multifunctional graphene microstructures inspired by honeycomb for ultrahigh performance electromagnetic interference shielding and wearable applications. *ACS Nano* 2021;15:8907-18. DOI PubMed
158. Yu W, Peng Y, Cao L, Zhao W, Liu X. Free-standing laser-induced graphene films for high-performance electromagnetic interference shielding. *Carbon* 2021;183:600-11. DOI
159. Tonouchi M. Cutting-edge terahertz technology. *Nat Photon* 2007;1:97-105. DOI
160. Zhang XC, Shkurinov A, Zhang Y. Extreme terahertz science. *Nat Photon* 2017;11:16-8. DOI
161. Jiang J, Guan Q, Liu Y, Sun X, Wen Z. Abrasion and fracture self-healable triboelectric nanogenerator with ultrahigh stretchability and long-term durability. *Adv Funct Mater* 2021;31:2105380. DOI
162. Zhu S, Yu G, Tang W, Hu J, Luo E. Thermoacoustically driven liquid-metal-based triboelectric nanogenerator: a thermal power generator without solid moving parts. *Appl Phys Lett* 2021;118:113902. DOI
163. Stanford MG, Li JT, Chyan Y, Wang Z, Wang W, Tour JM. Laser-induced graphene triboelectric nanogenerators. *ACS Nano* 2019;13:7166-74. DOI PubMed
164. Jiang C, Li X, Yao Y, et al. A multifunctional and highly flexible triboelectric nanogenerator based on MXene-enabled porous film integrated with laser-induced graphene electrode. *Nano Energy* 2019;66:104121. DOI
165. Yang L, Liu C, Yuan W, et al. Fully stretchable, porous MXene-graphene foam nanocomposites for energy harvesting and self-powered sensing. *Nano Energy* 2022;103:107807. DOI
166. Huang L, Xu S, Wang Z, et al. Self-reporting and photothermally enhanced rapid bacterial killing on a laser-induced graphene mask. *ACS Nano* 2020;14:12045-53. DOI PubMed
167. Zhang C, Chen H, Ding X, et al. Human motion-driven self-powered stretchable sensing platform based on laser-induced graphene foams. *Appl Phys Rev* 2022;9:011413. DOI
168. Shi X, Zhou F, Peng J, Wu R, Wu Z, Bao X. One-step scalable fabrication of graphene-integrated micro-supercapacitors with remarkable flexibility and exceptional performance uniformity. *Adv Funct Mater* 2019;29:1902860. DOI
169. Peng Z, Lin J, Ye R, Samuel EL, Tour JM. Flexible and stackable laser-induced graphene supercapacitors. *ACS Appl Mater Interfaces* 2015;7:3414-9. DOI PubMed
170. Li G, Mo X, Law W, Chan KC. 3D printed graphene/nickel electrodes for high areal capacitance electrochemical storage. *J Mater Chem A* 2019;7:4055-62. DOI
171. Li L, Zhang J, Peng Z, et al. High-performance pseudocapacitive microsupercapacitors from laser-induced graphene. *Adv Mater* 2016;28:838-45. DOI PubMed
172. Song W, Zhu J, Gan B, et al. Flexible, stretchable, and transparent planar microsupercapacitors based on 3D porous laser-induced graphene. *Small* 2018;14:1702249. DOI PubMed
173. Tehrani F, Beltrán-gastélum M, Sheth K, et al. Laser-induced graphene composites for printed, stretchable, and wearable electronics. *Adv Mater Technol* 2019;4:1900162. DOI
174. Alhajji E, Zhang F, Alshareef HN. Status and prospects of laser-induced graphene for battery applications. *Energy Technol* 2021;9:2100454. DOI
175. Gao X, Jia Y, Zhang W, Yuan C, Xu J. Mechanics-driven anode material failure in battery safety and capacity deterioration issues: a review. *Appl Mech Rev* 2022;74:060801. DOI
176. Ren M, Zhang J, Tour JM. Laser-induced graphene hybrid catalysts for rechargeable Zn-air batteries. *ACS Appl Energy Mater* 2019;2:1460-8. DOI
177. Ye R, Peng Z, Wang T, et al. In situ formation of metal oxide nanocrystals embedded in laser-induced graphene. *ACS Nano* 2015;9:9244-51. DOI PubMed
178. Zhang J, Ren M, Li Y, Tour JM. In situ synthesis of efficient water oxidation catalysts in laser-induced graphene. *ACS Energy Lett* 2018;3:677-83. DOI
179. Aslam S, Sagar RUR, Liu Y, et al. Graphene decorated polymeric flexible materials for lightweight high areal energy lithium-ion batteries. *Appl Mater Today* 2019;17:123-9. DOI

180. Yi J, Chen J, Yang Z, et al. Facile Patterning of laser-induced graphene with tailored li nucleation kinetics for stable lithium-metal batteries. *Adv Energy Mater* 2019;9:1901796. [DOI](#)
181. Duan W, Chen G, Chen C, et al. Electrochemical removal of hexavalent chromium using electrically conducting carbon nanotube/polymer composite ultrafiltration membranes. *J Membr Sci* 2017;531:160-71. [DOI](#)
182. Sha J, Li Y, Villegas Salvatierra R, et al. Three-dimensional printed graphene foams. *ACS Nano* 2017;11:6860-7. [DOI](#) [PubMed](#)
183. Luong DX, Subramanian AK, Silva GAL, et al. Laminated object manufacturing of 3D-printed laser-induced graphene foams. *Adv Mater* 2018;30:e1707416. [DOI](#) [PubMed](#)